Chemical Science

ROYAL SOCIETY OF CHEMISTRY

EDGE ARTICLE

View Article Online
View Journal | View Issue

Cite this: *Chem. Sci.*, 2022, **13**, 6373

All publication charges for this article have been paid for by the Royal Society of Chemistry

Ultrafast coherent photoexcited dynamics in a trimeric dendrimer probed by X-ray stimulated-Raman signals†

Victor M. Freixas, ‡[a] Daniel Keefer, ‡[b] Sergei Tretiak, [c] Sebastian Fernandez-Alberti [a] and Shaul Mukamel *[b]

The photoinduced ultrafast coherent inter-chromophore energy redistribution in a triarylamine trimer is explored using nonadiabatic excited state molecular dynamics followed by simulations of X-ray Raman signals. The nitrogencentered system ensures strong interchromophore interactions and, thus, the presence of coherences. Nevertheless, the multitude of non-deterministic photoinduced pathways during the ultrafast inter-branch migration of the excitation results in random confinement on some branches and, therefore, spatial exciton scrambling and loss of phase information at long times. We show that the vibronic coherence dynamics evolving into the incoherent scrambling mechanism on ultrafast 50 fs timescale, is accurately probed by the TRUECARS X-ray stimulated Raman signal. In combination with previous results, where the technique has revealed long-lived coherences in a rigid heterodimer, the signal is most valuable for detecting ultrafast molecular coherences or their absence. We demonstrate that X-ray Raman spectroscopy is a useful tool in the chemical design of functional molecular building blocks.

Received 28th January 2022
Accepted 11th April 2022

DOI: 10.1039/d2sc00601d

rsc.li/chemical-science

Introduction

Dendrimers are highly branched multichromophoric conjugated macromolecules with well-defined structural arrangements.[1–3] Their highly polarizable and spatially extended π-electron manifold controls their highly tunable photoexcited dynamics and potential applications. The efficiency of light harvesting and subsequent electronic and vibrational (vibronic) energy redistribution depends on the type of their constituent chromophore units, their structural organization in the connected branches, symmetry, and the energy funneling through different nonradiative relaxation channels.[4]

The energy transfer between dendritic branches can involve coherent[5] or incoherent[6] hopping mechanisms. While coherent processes involve in-phase evolution of spatially delocalized electronic wavefunctions, incoherent hopping-like mechanisms ultimately lead to a random exciton self-trapping and spatial scrambling on different units.[7–12] The competition between these two processes reflects the relative strengths of electronic couplings and thermal fluctuations.

Coherences can have either pure electronic or vibronic origin.[13,14] Electronic coherences are evaluated through the calculation of the pure dephasing time,[15,16] *i.e.*, the dephasing of the off-diagonal elements of the density matrix involving a mechanism which erodes the phase relationship between states without changing their population. On the other hand, vibronic coherences require the calculation of the full quantum wavefunction of electrons and nuclei as well as the corresponding nonadiabatic couplings between states.[14] Often, vibronic dynamics funnel the energy transfer through specific vibrational modes that modulate the wavelike localized – delocalized motion of the electronic wavefunction.[11] That is, the nonequilibrium dynamics of such selected excited vibrations is observed as ultrafast beatings of electronic populations.[17–24]

The choice of the dendrimer's branching unit allows a direct control of the inter-branch interactions and, therefore, the coherence between branches. This has significant effects on its spectroscopic properties. Nitrogen-centered dendrimers have been shown to induce stronger interactions and electronic delocalizations compared to benzene-centered ones.[5,10,25] The fast decay observed in ultrafast fluorescence anisotropy measurements performed on a triarylamine trimer supports the fact that coherence processes must be taken into account.[25] The photoexcitation and subsequent electronic and vibrational energy redistribution in large conjugated dendrimers involve dynamics in coupled excited states and multiple events like

[a]*Departamento de Ciencia y Tecnologia, Universidad Nacional de Quilmes/CONICET, B1876BXD, Bernal, Argentina*

[b]*Department of Chemistry and Physics and Astronomy, University of California, Irvine, California 92697-2025, USA. E-mail: smukamel@uci.edu*

[c]*Theoretical Division, Los Alamos National Laboratory, Los Alamos, New Mexico 87545, USA*

† Electronic supplementary information (ESI) available. See https://doi.org/10.1039/d2sc00601d

‡ These two authors contributed equally.

transient localization and delocalization of the wavefunction, coherent and incoherent inter-chromophore energy transfers, exciton self-trapping and internal conversion processes.[26] Such dynamics imply the passages through conical intersections that require quantum methods beyond Born–Oppenheimer approximation.[27,28]

Understanding coherence in dendrimers is a crucial challenge toward utilization of underpinning physical process for tailored chemical design. Over the past decade, sophisticated 2D electronic spectroscopy techniques[29,30] have been developed to provide time-resolved signatures of coherences.[31] More recently, X-ray free electron laser (XFEL) beam sources that offered unprecedented spatial, temporal and spectral resolutions,[32] making them novel probes of ultrafast chemical dynamics.[33,34] Pioneering experimental probes such as stimulated Raman transitions between electronic states[35] or (time-resolved) X-ray scattering-based measurements[36,37] have been demonstrated.

The theoretical design of new signals, and the prediction of their capabilities on molecular systems with distinct dynamics, is an important step in ultrafast X-ray sciences due to the extremely high cost and difficulty of the corresponding experiments. One promising signal that has been put forward recently, is the Transient Redistribution of Ultrafast Electronic Coherences in Attosecond Raman Signals (TRUECARS).[38,39] It uses a hybrid broadband + narrowband off-resonant X-ray probe field at delay time τ after the pump pulse that initiates a stimulated Raman process between two electronic states. The hybrid field – requiring precise phase control between the two pulses – can alternatively be substituted by a single stochastic XFEL pulse in a covariance-based measurement.[40] In either case, the signal is free from the usually dominating population dynamics and is finite only when there is a nuclear wavepacket overlap between electronic states. At short times, these coherences can be unique signatures of passages through conical intersections, since they are created due to wavepacket bifurcation. The signal is also a good indicator of whether the coherences survive multiple nonadiabatic passages, or whether they are destroyed by decoherence processes. We have previously simulated TRUECARS for the photoinduced dynamics in a rigid heterodimer, demonstrating that the signal can adequately monitor the experimentally observed long-living coherence surviving multiple conical intersection passages for several hundred femtoseconds at room temperature.[41]

In the present study, we perform excited state nonadiabatic molecular dynamics simulations of the triarylamine trimer depicted in Fig. 1a using the *ab initio* multiple cloning approach (AIMC).[42,43] The three equivalent branches of the dendrimer are connected by a nitrogen center that enhances the interaction and delocalization between states. According to previous ultrafast fluorescence anisotropy measurements, its fast decay cannot be reproduced using the Förster energy transfer model and coherences must be taken into account.[25] This implies using sophisticated computational techniques that consider transient strong coupling regimes and wavefunction delocalizations. Using information from AIMC calculations, we then simulate the non-linear X-ray TRUECARS signal to monitor the interplay between coherent and incoherent inter-chromophore energy redistribution regimes. Due to the fast energy exchange between the three branches, it is expected that coherences only persist during a few tens of femtoseconds, making this dendrimer an ideal system to test the capacity of AIMC and the TRUECARS signal to monitor coherences.

Results

We start with conformational sampling of the triarylamine trimer using equilibrated ground state molecular dynamics. It shows that phenylene ethynylene units can freely rotate at room temperature (Fig. 1b). Fig. 1c displays the simulated absorption spectra with separated contributions from different excited states S_1–S_{15}. The energies and spatial distribution of electronic transition densities of S_1, S_2 and S_3 reflect the 3-fold symmetry, that is, S_1, S_2 are degenerate at ground state minimum, while S_3 is fully delocalized at higher energy as shown by the respective orbital plots in the insets of Fig. 1c. The validity of the electronic structure method for phenylene–ethynylene dendrimer in question is justified by a good agreement with the experimental absorption spectra[25] and consistency with the Frenkel exciton Hamiltonian typically used for these systems.

The time evolution of the expectation values of the electronic state populations[42,44] are shown in Fig. 2a. According to Fig. 1c, an initial laser excitation at 388 nm populates the excited states S_1 and S_2 with a negligible contribution from S_3. An efficient energy transfer to S_1 then takes place within the first 100 fs. Different processes take place during that time. An exponential decay from S_2 to S_1 is concomitant with a damped oscillatory interchange between these states. These two behaviors of the population transfer are due to two different effects introduced by the energy transfer between these states. To analyze them, the increase of S_1 population in time has been fitted to the equation:

$$f(t) = a + \frac{b-a}{2}\left\{\exp\left(-\frac{t}{\tau_1}\right) + \frac{1}{2}\left[1+\cos\left(2\pi\frac{t}{T}\right)\right]\exp\left(-\frac{t}{\tau_2}\right)\right\}. \quad (1)$$

The parameters from this fitting are given in supplementary Table S1.† On one hand, after each crossing of the S_2/S_1 seam, the molecular system follows different pathways on either the S_1 or S_2 potential energy surfaces. The nuclear motion on the S_1 state moves the molecular system away to regions of low coupling, while the nuclear motion on S_2 keeps it lingering in the regions of strong coupling, which facilitates subsequent relaxation to S_1. This behavior, previously reported in other branched dendritic molecules,[45,46] leads to the ultimate exponential decay of the initial S_2 electronic population to S_1. It is represented by the pure decoherence time $\tau_1 = 5.42$ fs that corresponds to the decoherence time $\tau = 4.94$ fs obtained from the pure dephasing rate D_{12} calculated using the autocorrelation function within linear response theory[14,15] (eqn S14†). The corresponding curve is shown in supplemental Fig. S3.† On the other hand, the direction of energy transfer between S_2 and S_1, represented by the non adiabatic couplings (NACR), does not

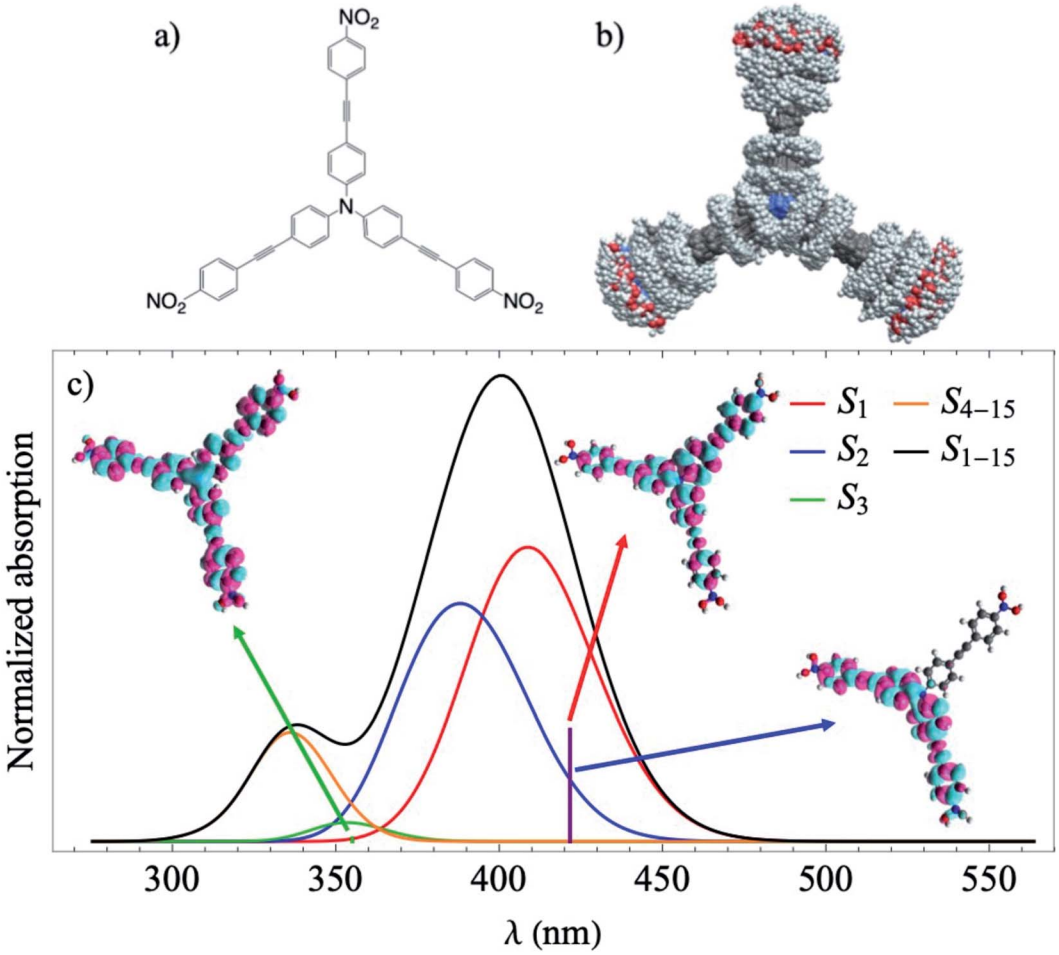

Fig. 1 (a) Chemical structure of the triarylamine trimer; (b) superposition of structural snapshots obtained from ground state molecular dynamics at ambient conditions, the color convention followed for the atomic species is: white for hydrogen, gray for carbon, blue for nitrogen and red for oxygen; (c) simulated absorption spectrum (black) with separated contributions (colors) from the different excited states. Vertical lines mark values obtained at ground state minimum, and the corresponding spatial distribution of electronic transition densities of S_1, S_2 and S_3, calculated for the ground state energy minimum, are shown in the insets. The oscillator strength corresponding to S_3 vertical line was magnified by 3 orders of magnitude.

involve a random participation of all vibrational motions, but of a reduced set of vibrational modes with periods of ~20 fs (see Fig. S4c†). This manifests in Fig. 2a as oscillation patterns of the S_2 and S_1 electronic populations with periods of ~20 fs, which therefore are associated to vibronic coherences with the vibronic decoherence time $\tau_2 = 23.31$ fs.

Localization patterns of the transition densities associated with intra- and inter-branch energy transfers are mediated by thermal fluctuations at room temperature within the same electronic state or by energy transfers between different electronic states. Therefore, the time evolution of the electronic populations shown in Fig. 2a is not necessarily related to inter-branch energy transfer. This is evident from Fig. 2b that shows the average fraction of electronic transition density localized on the different branches. The formal definition of fraction of transition density is provided in the ESI (eqn S11†). In each trajectory we label the three branches as A, B, and C according to their decreasing order of fraction of transition density at $t = 0$. During the first ~100 fs, the excess of electronic energy leads to an ultrafast inter-branch migration. The absence of an energy gradient leads to an ultrafast energy redistribution among isoenergetic branches. Thus, we observe a final scrambling of the spatial electronic transition density due to incoherent dynamic mechanisms governed by thermal fluctuations. This process competes with the concerted evolution of the nuclear wavepackets in S_1 and S_2 that modulates the strength and longevity of the vibronic coherence. Considering coupling as one third of the energy splitting between S_1/S_2 and S_3 calculated at ground state minimum, a value of 1484 cm^{-1} was obtained. The strength of the thermal fluctuations, calculated as the full width at half maximum of the excitation energy, results in 2000 cm^{-1} and 2250 cm^{-1} for S_1 and S_2 respectively. That is, thermal fluctuations compete with coupling by randomly distorting the equivalent branches and breaking their symmetry, which leads to persistent interbranch exciton exchanges throughout the simulations. Despite that, the coupling is large enough to guarantee certain initial coherence.

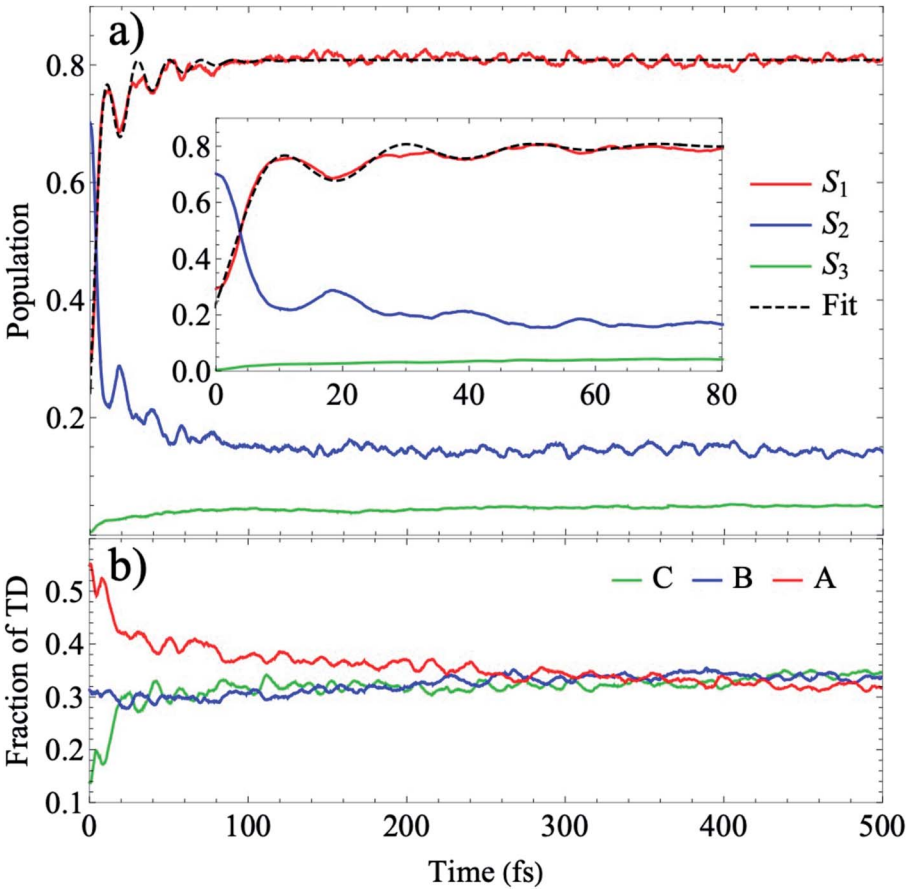

Fig. 2 (a) Time evolution of the electronic populations averaged over the ensemble of AIMC simulations according to the expectation values calculated according to (eqn S18†). The inset shows the oscillations of S_1 and S_2 at earlier times. The dashed black line is the fit to the $f(t)$ function given by eqn (1); (b) time evolution of the mean fraction of electronic transition density localized on the different branches. For each trajectory we label the three branches as A, B, and C according to their decreasing order of fraction of transition density at $t = 0$.

It is worth pointing out that previous studies using the trajectory surface hopping protocol, in a similar system but with a benzene being the branching center, totally miss the oscillation patterns observed in this work.[47] This difference is attributed to partially stronger couplings introduced by the nitrogen-center that increase the interaction and delocalization between states, as well as the superior AIMC method able to properly describe coherent dynamics in contrast with ad hoc nature of trajectory surface hopping method. In order to clarify this issue, surface hopping simulations of the triarylamine trimer were performed. Results are shown in supplemental Fig. S4.† The evolution in time of S_1 and S_2 populations do not reproduce the oscillation patterns shown in Fig. 2a, pointing out the limitation of this method to properly evidenciate vibronic coherences.

Our analysis of individual trajectories indicates that the spatial scrambling corresponding to the ensemble-average values shown in Fig. 2b is due to random transfers between linear branches rather than to a complete delocalization of the wavefunction across the entire molecule. This is clearly evident from Fig. 3 that shows results for AIMC trajectory 1, which is typical for the majority of trajectories in the ensemble. We observe that population exchanges between S_1 and S_2 states involve sudden changes in the transition density spatial localization. While transient delocalizations take place at the moments of energy transfer between states and induce energy transfer between different branches, the final result is a random exciton self-trapping on one or two branches, with the fraction of transition density not necessarily related to the initial order. Since the identity of the branches is defined at $t = 0$, the random exciton self-trapping reflects as a deceiving equivalence between the fraction of transition density on the branches at the end of the simulation, as shown in Fig. 2b. The electronic transition density matrices that correspond to the different snapshots indicated in Fig. 3a, are depicted in supplemental Fig. S5.† In agreement with Fig. 3a, we can observe a transient delocalization of the electronic transition density within the branches A and B at 6.4 fs, accompanied by a population exchange between S_1 and S_2. Subsequently, the transition density is localized on the branch A and a new transient delocalization between the branches A and C takes place at $t = 22.6$ fs. The excitation finally relaxed to S_1 and becomes localized on the C branch.

Thus, the successive transient couplings between states through multitude of non-deterministic photoinduced pathways involve delocalizations of pairs of different branches that

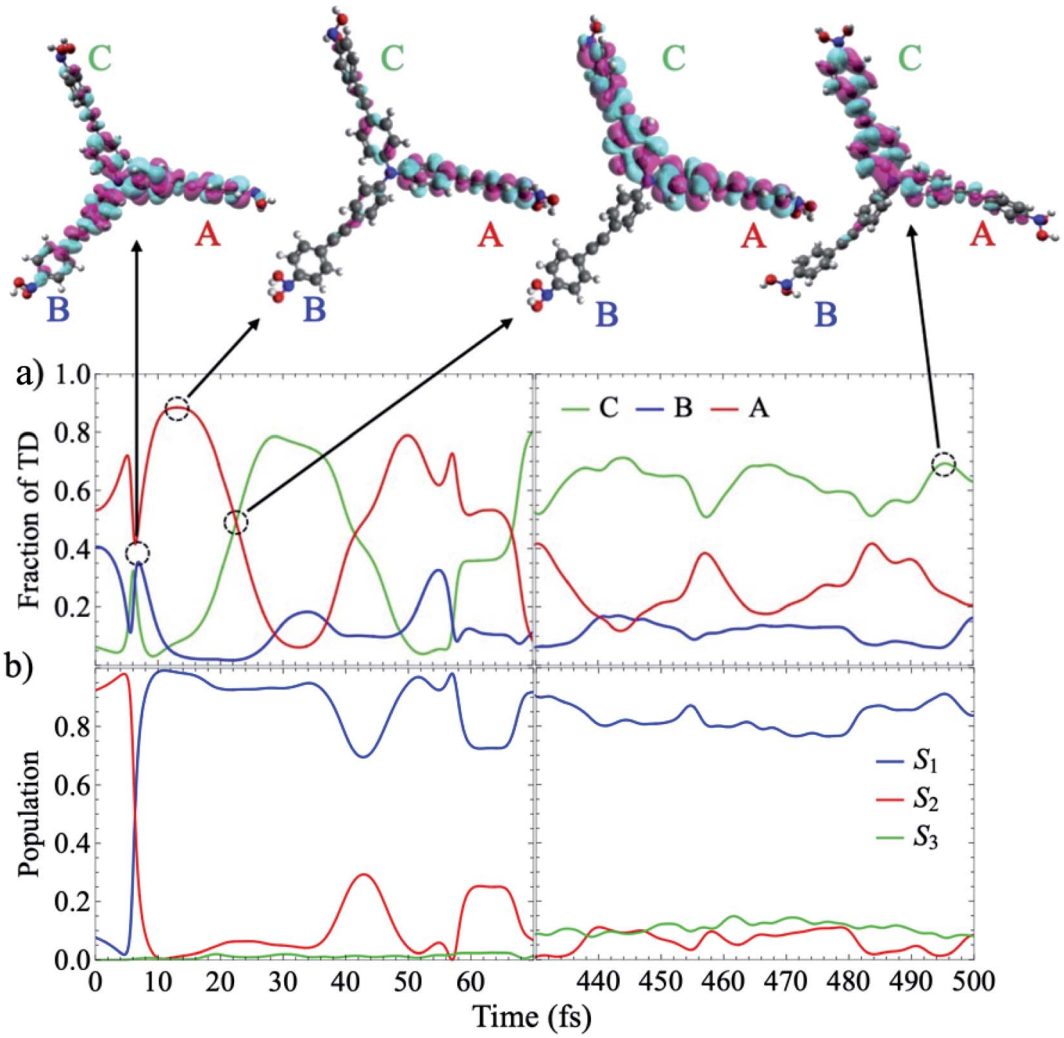

Fig. 3 Dynamics in a typical trajectory 1. (a) Temporal evolution of the fraction of transition density over each branch. Labels A, B, and C are assigned according to the decreasing order of fraction of transition density at $t = 0$. Selected snapshots of the transition densities in real space are also shown. (b) Concomitant electronic population evolution for the same AIMC trajectory.

ultimately leads to an exciton self-trapping on one within a random molecular scrambling. Furthermore, as shown in supplemental Fig. S6,† these transient couplings driving the vibronic dynamics are assisted by a reduced set of high-frequency normal modes.

We next examine the possibility to probe the coherence dynamics of the triarylamine trimer with the TRUECARS X-ray stimulated Raman signal, given by:

$$S(\omega_R, \tau) = 2\mathcal{I} \int_{-\infty}^{\infty} dt\, e^{i\omega_R(t-\tau)} \varepsilon_0^*(\omega_R)\varepsilon_1(t-\tau) \times \langle \Psi(t)|\hat{\alpha}|\Psi(t)\rangle, \quad (2)$$

where ε_0 and ε_1 are broadband and narrowband pulses, ω_R is the observed Raman frequency, and $\mathcal{I}$ denotes the imaginary part. The time-dependent polarizability $\langle\alpha\rangle$ is taken to be constant in the nuclear space, following the original formulation,[38] so each matrix element factorizes into the wavepacket overlap between the involved electronic states given in eqn (5).

The probe fields are kept off-resonant with any real valence-to-core transitions. Otherwise the populations will start to contribute and dominate the coherences. We have previously found that an ideal scenario to maximize the experimental cross-section is to choose the central frequency near a valence-to-core resonance, while still staying off-resonant (pre resonant).[40,41] Our molecule, shown in Fig. 1a, offers carbon, nitrogen and oxygen species as potential candidates. Another possibility to enhance the intrinsically weak coherence contribution and overcome potential loss channels like ionization or Auger–Meitner decay, is to use tailored light fields that steer the molecular wavepacket motion by coherent control.[48]

X-ray TRUECARS initiates a stimulated Raman process between electronic states, similar to Raman spectroscopy between vibrational levels in the visible domain.[33] Only the ensemble average over all trajectories is experimentally observable. It is however useful to first discuss individual trajectories to gain insight about the underlying mechanisms. One example is depicted in Fig. 4 for a representative trajectory

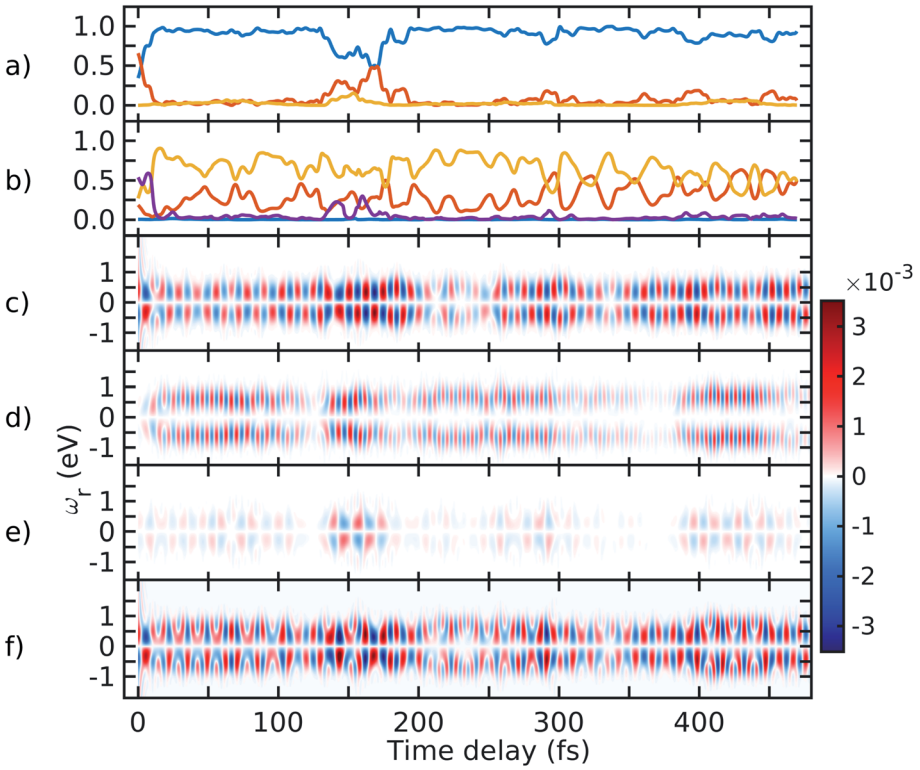

Fig. 4 Dynamics and TRUECARS signal in trajectory 2. (a) Populations in the S_1 (blue), S_2 (red) and S_3 (yellow) states. (b) Fraction of transition density in branch A (purple), B (yellow), C (red) and around the central nitrogen (blue). (c) Frequency-dispersed TRUECARS signal (eqn (2)) for the coherence ρ_{12} between S_1 and S_2. (d and e) same as (c) for ρ_{13} and ρ_{23}. (f) Total TRUECARS signal for trajectory 2 given by the sum of (c–e).

2. Following an initial population transfer from S_2 to S_1, there is a free 100 fs evolution period. At 150 fs, the molecule again enters a region of strong nonadiabatic coupling, with population exchange between all three states (although S_3 is only slightly affected). The transition density fractions in Fig. 4b exhibit the typical fluctuations, with the majority of excitation being located in branches B and C after a short redistribution period at the beginning of the dynamics.

Since three electronic states are involved, there exist three coherences ρ_{12}, ρ_{13} and ρ_{23}. A TRUECARS signal according to eqn (2) can be calculated for each of these coherences, and their sum gives the total signal of the trajectory. According to Fig. 4, the contribution from the ρ_{12} coherence is the strongest. Interestingly, it is not only strong during the times when the molecule enters strong coupling regions – around 150–200 fs – but also in between. This suggests a concerted wavepacket evolution in the electronic states, where cloning events do not necessarily lead to decoherence. The signal contribution from the ρ_{13} coherence is only slightly weaker, and is located at the higher Raman shifts, in agreement with the larger S_3–S_1 energy difference compared to S_2–S_1. The ρ_{23} contribution is the weakest, as these two states are much less populated than S_1 throughout the dynamics. The signal exhibits considerable magnitude only around 150 fs, where both S_2 and S_3 get significantly populated intermediately.

Trajectory 2 illustrates the characteristics of a large fraction of trajectories in the ensemble. The domination of the ρ_{12} contribution to the signal (given degeneracy of S_1 and S_2 states due to molecular symmetry), as well as the trapping of transition density in two of the three branches, is typical. Three additional trajectories shown in supplemental Fig. S7–S9† exhibit the largest differences to give insight about the variance within the ensemble. Individual features – like the magnitude of

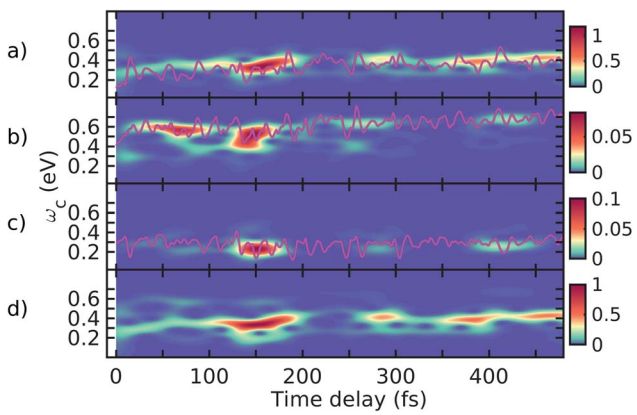

Fig. 5 Spectrogram of the TRUECARS signal (eqn (6)), dissected into the three contributions. (a) Spectrogram of the ρ_{12} coherence signal in Fig. 4c. (b) Spectrogram of the ρ_{13} coherence signal in Fig. 4d. (c) Spectrogram of the ρ_{23} coherence signal in Fig. 4e. The pink lines show the energy splitting between the corresponding adiabatic states as extracted from the AIMC simulations. (d) Spectrogram of the total signal in Fig. 4f.

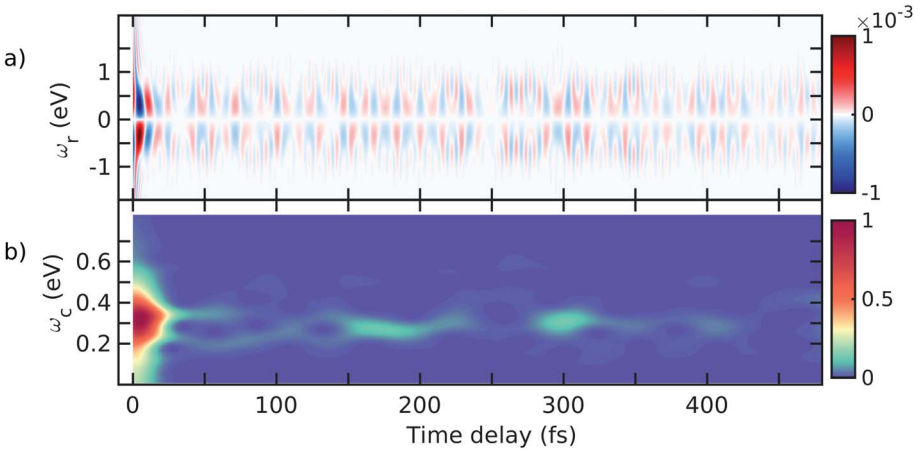

Fig. 6 (a) TRUECARS signal (eqn (2)) of the ensemble, obtained by averaging the over all 300 trajectories. (b) Spectrogram of the TRUECARS signal (eqn (6)).

population transfer, the relative magnitude of the coherence contributions or the branches where the transition density is eventually trapped – may vary, but the qualitative structure persists.

The spectrogram of the TRUECARS signal $I(\omega_c, \tau)$[39] (eqn (6)) gives the vibronic coherence distribution and corresponds to the energetic splitting of the adiabatic electronic states. $I(\omega_c, \tau)$ is depicted in Fig. 5 for trajectory 2, dissected into the three coherences similar to Fig. 4. The spectrogram of each contribution correctly reproduces the energy splitting of the involved adiabatic electronic states, with S_2–S_1 and S_3–S_2 oscillating between 0 and 0.4 eV, and S_3–S_1 oscillating between 0.4 and 0.8 eV. Both contributions are visible in the total spectrogram depicted in Fig. 5d, with the dominating feature around 0.3 eV and the weaker S_3–S_1 signal at higher ω_c. The spectrograms along other trajectories (not shown) are very similar.

In Fig. 6, we present the total TRUECARS signal averaged over all 300 trajectories. Surprisingly, even though the individual trajectories exhibit persisting coherences throughout the dynamics, the total signal is strong only in the very beginning and rapidly decays. This is in agreement with Fig. 2, where the population transfer as well as the transition density relocalization complete over after 50–100 fs. The spectrogram shown in Fig. 6 exhibits the main feature centered around 0.3 eV, with additional weak features stemming mainly from the ρ_{13} coherence at higher Raman shifts. This dynamics is in a stark contrast to the rigid heterodimer previously investigated,[41] where the experimentally observed long-living coherences are correctly reproduced in the ensemble-averaged TRUECARS signal. In the present molecule, we observe a rapid decay of the coherence, corresponding to the incoherent scrambling of the transition density across all three arms. This corroborates that TRUECARS can be a powerful tool in the molecular design of future optoelectronic devices on the basis of such dendritic or multi-chromophoric building blocks, where coherent electronic evolution is advantageous for conversion efficiencies. As demonstrated here, TRUECARS can directly monitor whether or not such coherence properties are present in a given molecule.

Conclusions

The photoexcitation and subsequent inter-branch energy redistribution of the triarylamine trimer shown in Fig. 1a have been simulated using AIMC that treats decoherences in a natural way beyond the Born–Oppenheimer dynamics on several excited states. The photophysics of this trimer results in a competition between coherent and incoherent energy transfers between branches. An initial ultrafast coherent dynamics is followed by incoherent mechanisms governed by thermal fluctuations that ultimately lead to a random molecular scrambling. Successive transient couplings creates multitude of non-deterministic photoinduced pathways involving delocalizations of pairs of different branches that ultimately leads to an exciton self-trapping on one within a random molecular scrambling. This is a consequence of the fact that thermal fluctuations compete with coupling differentially and randomly distorting the equivalent branches, which leads to persistent interbranch exciton exchanges throughout the simulations. Despite that, the coupling seems to be relatively large enough to guarantee certain initial coherence. Two distinct coherences, *i.e.*, pure electronic and vibronic coherences, can be distinguished at earlier times. Vibronic couplings principally involve asymmetric motions in two of the three branches per time and are related to specific high-frequency bond-stretching vibrational modes (supplemental Fig. S6†).

We have calculated the TRUECARS X-ray stimulated Raman signal for all individual trajectories as well as the ensemble average of the AIMC dynamics. TRUECARS is an unambiguous probe of molecular vibronic coherences as it is free from the usually dominating population background. The signal is strong only at the very beginning of the dynamics and rapidly decays within the first 50 femtoseconds, reproducing the incoherent scrambling dynamics of the photoexcited triarylamine trimer. This is different from previous results on a bichromophoric heterodimer,[41] where TRUECARS has revealed long-living coherences that were also experimentally observed. This demonstrates the unique capability of near-future XFEL

experiments in monitoring coherent molecular dynamics, and thereby help in the chemical design of molecular building blocks for optoelectronic materials that benefit from these coherences. While coherent TRUECARS, as calculated here, requires phase control of the two pulses in the hybrid probe field, the information is equally accessible by a covariance-based measurement with an existing single stochastic XFEL pulse.[40]

Methods

AIMC simulations

The *ab initio* multiple cloning (AIMC)[42,43] technique is an extension of the Multiconfigurational Ehrenfest (MCE) method[49–51] that uses trajectory-guided Gaussian basis functions (TBF). Independent Ehrenfest trajectories, *i.e.* configurations $\psi_n(t)$ are used as a basis set to represent the full time-dependent quantum-mechanical wavefunction of electrons and nuclei:

$$|\Psi(t)\rangle = \sum_n c_n |\psi_n(t)\rangle \tag{3}$$

with:

$$|\psi_n(t)\rangle = |\chi_n\rangle \left(\sum_I a_I^{(n)}(t) \left| \phi_I^{(n)} \right\rangle \right) \tag{4}$$

where $\chi_n(t)$ and $\phi_I^{(n)}$ are the nuclear and electronic components, respectively.

$\chi_n(t)$ are coherent states[52,53] given by frozen Gaussian functions centered in the Ehrenfest trajectories. In the original versions of MCE and AIMC,[51] $\phi_I^{(n)}$ are adiabatic states. However, photoinduced dynamics in large conjugated molecules like dendrimers can involve unavoided crossings between states whose nonadiabatic couplings have sharp peaks strongly localized in configurational space.[54–56] In these situations, the adiabatic states change abruptly within the Gaussian width and the molecule should follow the diabatic pathways. Otherwise, unphysical intramolecular energy redistributions can occur. To address this issue, we use time-dependent diabatic electronic states, defined to coincide with adiabatic states in the center of each Gaussian,[54–56] as detailed elsewhere.[51]

Ehrenfest trajectories evolve on an average potential energy surface that can lead to unphysical nuclear motions if the intramolecular energy redistribution follows different relaxation pathways dominated by several electronic states whose forces are very different. In these situations, the original wavefunction branches out into multiple parts, each following a specific pathway. AIMC quantifies them by using a set of cloning criteria.[42,57] When these criteria are met, the original Ehrenfest trajectory splits into two new trajectories that continue their dynamics with the same nuclear wave function at the moment of cloning event but different electronic populations in order to be independently propagated on different potential energy surfaces. Such cloning events introduce decoherence in a natural way for wavefunctions moving on sufficiently different potential energy surfaces. More details and technical aspects of the AIMC method can be found elsewhere.[42,43,57,58]

The AIMC method is implemented within the nonadiabatic excited state molecular dynamics (NEXMD) framework.[42,59,60] It is worth mentioning that the *ab initio* from AIMC comes from historical reasons and the method can be adapted either to TDDFT[61] or semiempirical calculations as is the case of NEXMD. The NEXMD implementation has been specifically developed to deal with photoinduced dynamics in large multichormophoric conjugated molecules involving several coupled electronic excited states. Excited states energies,[62–64] gradients[65,66] and nonadiabatic couplings[67–69] are calculated on-the-fly at the configuration interaction singles (CIS) level of theory using the semiempirical Austin Model 1 (AM1) Hamiltonian[70] with the Collective Electronic Oscillator (CEO) approach.[71–73] In our previous studies we have tested this approach for a number of dendritic chromophores, where we have found semi-quantitative agreement with experimental data and higher level electronic structure methodologies.[45–47,59,62] Furthermore, the accuracy of this AIMC implementation has been previously tested on photoinduced nonadiabatic energy transfer pathways dynamics in poly(phenylene ethynylene) dendrimer building blocks.[74]

AIMC trajectories start by vertical excitation of 300 initial configurations equispaced in time obtained from a 1 ns equilibrated ground state molecular dynamics simulation. This simulation was performed at ambient conditions (T = 300 K) using the Langevin thermostat with a friction coefficient $\gamma = 2.0$ ps^{-1} and a time step of 0.5 fs starting from an initial structure that has been previously minimized using the generalized amber force field[75] followed by a subsequent second minimization using AM1. The initial excited states were populated according to a Franck–Condon window given by $g_{\mathrm{I}}(r, R) = f_{\mathrm{I}} \exp[-T^2(E_{\mathrm{laser}} - E_{\mathrm{I}})^2]$ where f_{I} and E_{I} are the oscillator strength and energy of excited state I, and E_{laser} is the energy of a Gaussian laser pulse $f(t) = \exp(-t^2/2T^2)$, centered at 388 nm that corresponds to the maximum of the absorption for the S_2 state, and T = 42.5 fs, *i.e.*, a FWHM = 100 fs. AIMC trajectories were run at constant energy and with a 0.05 fs time step. Gaussian widths were taken from the optimized parameters reported by Thompson *et al.*[76] Details on the cloning criteria and thresholds can be found in the ESI.†

The coherence between any two electronic states K and L can be extracted from AIMC simulations as:

$$\rho_{\mathrm{KL}} = \frac{1}{2} \sum_{m,n} c_m^* c_n \langle \chi_m | \chi_n \rangle \sum_I \Big[\left(a_{\mathrm{K}}^{(m)}\right)^* a_{\mathrm{I}}^{(n)} \langle \phi_{\mathrm{L}}^{(m)} | \phi_{\mathrm{I}}^{(n)} \rangle + \left(a_{\mathrm{I}}^{(m)}\right)^* a_{\mathrm{L}}^{(n)} \langle \phi_{\mathrm{I}}^{(m)} | \phi_{\mathrm{K}}^{(n)} \rangle \Big]. \tag{5}$$

It includes coherences between the electronic and the nuclear subsystem, each carrying their own phases. Their joint information is required to obtain a TRUECARS signal, and their state is accounted for in the molecular wavefunction when calculating ρ_{KL}.

TRUECARS signal spectrogram

The TRUECARS signal given by eqn (2), was calculated with the broadband 500 attosecond pulse ε_0 and the narrowband 3 fs

pulse ε_1. A powerful analysis tool that is experimentally available for the TRUECARS signal is its spectrogram I.[39] This is a post-processing analysis using a gating function E_{gate} convoluted with a TRUECARS signal trace $S(t)$ at constant Raman shift ω_R (integration over positive or negative ω_R is also possible, while integration over the whole ω_R range yields zero). It is given by:

$$I(\omega_c, \tau_{coh}) = \left| \int_{-\infty}^{\infty} d\tau S(\tau) E_{\text{gate}}(\tau - \tau_{coh}) e^{-i\omega_c \tau} \right|^2 \quad (6)$$

and yields the transient frequency pattern of the signal oscillations.

Data availability

The data that supports the findings of this study are available within the ESI† and from the corresponding author upon reasonable request.

Author contributions

S. T., S. F.-A. and S. M. designed the project. V. M. F. and S. F.-A. performed AIMC simulations. D. K. calculated the signals and the Wigner spectrograms. All authors analyzed and interpreted the results. V. M. F. and D. K. prepared the figures. The manuscript was written with contributions from all authors. All authors were involved in the scientific discussion of the results of the paper. V. M. F. and D. K. contributed equally.

Conflicts of interest

There are no conflicts to declare.

Acknowledgements

We gratefully acknowledge support from the Chemical Sciences, Geosciences, and Bio-Sciences Division, Office of Basic Energy Sciences, Office of Science, US Department of Energy (DOE), through award DE-SC0019484 and under Triad National Security, LLC ("Triad") contract grant # 89233218CNA000001 (FWP: LANLE3T1). The work at Los Alamos National Laboratory (LANL) was performed in part at the Center for Integrated Nanotechnologies (CINT), a U.S. DOE User Facility. This research used resources provided by the LANL Institutional Computing Program. D. K. gratefully acknowledges support from the Alexander von Humboldt foundation through the Feodor Lynen program. S. F.-A. and V. M. F acknowledge support of CONICET, UNQ and ANPCyT (PICT-2018-02360).

References

1 V. Balzani, P. Ceroni, M. Maestri and V. Vicinelli, Light-harvesting dendrimers, *Curr. Opin. Chem. Biol.*, 2003, **7**, 657–665.
2 A. Nantalaksakul, D. Reddy, C. Bardeen and S. Thayumanavan, Light Harvesting Dendrimers, *Photosynth. Res.*, 2006, **87**, 133–150.
3 A. De Sio, X. T. Nguyen and C. Lienau, A new approach to light-harvesting with dendritic antenna, *Thin Solid Films*, 1998, **331**, 254–258.
4 D. L. Andrews, Light harvesting in dendrimer materials: Designer photophysics and electrodynamics, *J. Mater. Res.*, 2012, **27**, 627–638.
5 J. M. Lupton, I. D. W. Samuel, P. L. Burn and S. Mukamel, Control of intrachromophore excitonic coherence in electroluminescent conjugated dendrimers, *J. Phys. Chem. B*, 2002, **106**, 7647–7653.
6 T. Förster, Energiewanderung und fluoreszenz, *Naturwissenschaften*, 1946, **33**, 166–175.
7 J. Galindo, E. Atas, A. Altan, D. Kuroda, S. Fernandez-Alberti, S. Tretiak, A. Roitberg and V. Kleiman, Dynamics of Energy Transfer in a Conjugated Dendrimer Driven by Ultrafast Localization of Excitations, *J. Am. Chem. Soc.*, 2015, **137**, 11637–11644.
8 F. Ricci, T. Kim, W. Gao, Y. Lin, C.-Q. Ma and T. Goodson, Coherent energy and charge transport processes in oligothiophene dendrimers probed in solution and in the solid state with time-resolved spectroscopy and microscopy methods, *J. Phys. Chem. C*, 2019, **123**, 23419–23426.
9 M. C. Aguilera, A. E. Roitberg, V. D. Kleiman, S. Fernandez-Alberti and J. F. Galindo, Unraveling Direct and Indirect Energy Transfer Pathways in a Light-Harvesting Dendrimer, *J. Phys. Chem. C*, 2020, **124**, 22383–22391.
10 O. Varnavski, I. D. W. Samuel, L. O. Plsson, P. L. Burn and T. Goodson, Investigations of excitation energy transfer and intramolecular interactions in a nitrogen corded distyrylbenzene dendrimer system, *J. Chem. Phys.*, 2002, **116**, 8893–8903.
11 T. R. Nelson, D. Ondarse-Alvarez, N. Oldani, B. Rodriguez-Hernandez, L. Alfonso-Hernandez, J. F. Galindo, V. D. Kleiman, S. Fernandez-Alberti, A. E. Roitberg and S. Tretiak, Coherent exciton-vibrational dynamics and energy transfer in conjugated organics, *Nat. Commun.*, 2018, **9**, 2316.
12 D. Ondarse-Alvarez, N. Oldani, A. E. Roitberg, V. D. Kleiman, S. Tretiak and S. Fernandez-Alberti, Energy transfer and spatial scrambling of an exciton in a conjugated dendrimer, *Phys. Chem. Chem. Phys.*, 2018, **20**, 29648–29660.
13 T. Aida, D.-L. Jiang, E. Yashima and Y. Okamoto, Signatures of strong vibronic coupling mediating coherent charge transfer in two-dimensional electronic spectroscopy, *Z. Naturforsch., A: Phys. Sci.*, 2019, **74**, 721–737.
14 V. M. Freixas, S. Tretiak, D. V. Makhov, D. Shalashilin and S. Fernandez-Alberti, Vibronic quantum beating between electronic excited states in a heterodimer, *J. Phys. Chem. B*, 2020, **124**, 3992–4001.
15 S. Mukamel, *Principles of nonlinear optical spectroscopy*, Oxford University Press New York, 1995, vol. 29.
16 R. Hildner, D. Brinks and N. F. van Hulst, Femtosecond coherence and quantum control of single molecules at room temperature, *Nat. Phys.*, 2011, **7**, 172–177.
17 A. Kolli, E. J. O'Reilly, G. D. Scholes and A. Olaya-Castro, The fundamental role of quantized vibrations in coherent light harvesting by cryptophyte algae, *J. Chem. Phys.*, 2012, **137**, 174109.

18 E. J. O'Reilly and A. Olaya-Castro, Non-classicality of the molecular vibrations assisting exciton energy transfer at room temperature, *Nat. Commun.*, 2014, **5**, 3012.
19 S. Siwiak-Jaszek and A. Olaya-Castro, Transient synchronisation and quantum coherence in a bio-inspired vibronic dimer, *Faraday Discuss.*, 2019, **216**, 38–56.
20 H. Chen, X. Wang, C.-M. Han and H.-R. Li, Phonon-Mediated Excitation Energy Transfer in a Detuned Multi-Sites System, *J. Phys. B: At., Mol. Opt. Phys.*, 2019, **52**, 075501.
21 I. B. Juhász and Á. I. Csurgay, Impact of Undamped and Damped Intramolecular Vibrations on the Efficiency of Photosynthetic Exciton Energy Transfer, *AIP Adv.*, 2018, **8**, 045318.
22 R. Stones and A. Olaya-Castro, Vibronic Coupling as a Design Principle to Optimize Photosynthetic Energy Transfer, *Chem*, 2016, **1**, 822–824.
23 Z. Zhang and J. Wang, Origin of Long-Lived Quantum Coherence and Excitation Dynamics in Pigment-Protein Complexes, *Sci. Rep.*, 2016, **6**, 37629.
24 H.-B. Chen, P.-Y. Chiu and Y.-N. Chen, Vibration-Induced Coherence Enhancement of the Performance of a Biological Quantum Heat Engine, *Phys. Rev. E: Stat. Phys., Plasmas, Fluids, Relat. Interdiscip. Top.*, 2016, **94**, 052101.
25 O. P. Varnavski, J. C. Ostrowski, L. Sukhomlinova, R. J. Twieg, G. C. Bazan and T. Goodson, Coherent Effects in Energy Transport in Model Dendritic Structures Investigated by Ultrafast Fluorescence Anisotropy Spectroscopy, *J. Am. Chem. Soc.*, 2002, **124**, 1736–1743.
26 T. Nelson, S. Fernandez-Alberti, A. E. Roitberg and S. Tretiak, Nonadiabatic excited-state molecular dynamics: Modeling photophysics in organic conjugated materials, *Acc. Chem. Res.*, 2014, **47**, 1155–1164.
27 G. a. Worth and L. S. Cederbaum, Beyond Born-Oppenheimer: molecular dynamics through a conical intersection, *Annu. Rev. Phys. Chem.*, 2004, **55**, 127–158.
28 W. Domcke and D. R. Yarkony, Role of conical intersections in molecular spectroscopy and photoinduced chemical dynamics, *Annu. Rev. Phys. Chem.*, 2012, **63**, 325–352.
29 S. Mukamel, Multidimensional femtosecond correlation spectroscopies of electronic and vibrational excitations, *Annu. Rev. Phys. Chem.*, 2000, **51**, 691–729.
30 D. M. Jonas, Two-dimensional femtosecond spectroscopy, *Annu. Rev. Phys. Chem.*, 2003, **54**, 425–463.
31 T. Brixner, J. Stenger, H. M. Vaswani, M. Cho, R. E. Blankenship and G. R. Fleming, Two-dimensional spectroscopy of electronic couplings in photosynthesis, *Nature*, 2005, **434**, 625–628.
32 J. Duris, S. Li, T. Driver, E. G. Champenois, J. P. MacArthur, A. A. Lutman, Z. Zhang, P. Rosenberger, J. W. Aldrich, R. Coffee, et al., Tunable isolated attosecond x-ray pulses with gigawatt peak power from a free-electron laser, *Nat. Photonics*, 2020, **14**, 30–36.
33 S. Mukamel, D. Healion, Y. Zhang and J. D. Biggs, Multidimensional attosecond resonant x-ray spectroscopy of molecules: Lessons from the optical regime, *Annu. Rev. Phys. Chem.*, 2013, **64**, 101–127.
34 L. Young, K. Ueda, M. Gühr, P. H. Bucksbaum, M. Simon, S. Mukamel, N. Rohringer, K. C. Prince, C. Masciovecchio, M. Meyer, et al., Roadmap of ultrafast x-ray atomic and molecular physics, *J. Phys. B: At., Mol. Opt. Phys.*, 2018, **51**, 032003.
35 J. T. O'Neal, E. G. Champenois, S. Oberli, R. Obaid, A. Al-Haddad, J. Barnard, N. Berrah, R. Coffee, J. Duris, G. Galinis, et al., Electronic population transfer via impulsive stimulated x-ray Raman scattering with attosecond soft-x-ray pulses, *Phys. Rev. Lett.*, 2020, **125**, 073203.
36 J. Küpper, S. Stern, L. Holmegaard, F. Filsinger, A. Rouzée, A. Rudenko, P. Johnsson, A. V. Martin, M. Adolph, A. Aquila, et al., X-ray diffraction from isolated and strongly aligned gas-phase molecules with a free-electron laser, *Phys. Rev. Lett.*, 2014, **112**, 083002.
37 M. Minitti, J. Budarz, A. Kirrander, J. Robinson, D. Ratner, T. Lane, D. Zhu, J. Glownia, M. Kozina, H. Lemke, et al., Imaging molecular motion: Femtosecond x-ray scattering of an electrocyclic chemical reaction, *Phys. Rev. Lett.*, 2015, **114**, 255501.
38 M. Kowalewski, K. Bennett, K. E. Dorfman and S. Mukamel, Catching conical intersections in the act: Monitoring transient electronic coherences by attosecond stimulated x-ray Raman signals, *Phys. Rev. Lett.*, 2015, **115**, 193003.
39 D. Keefer, T. Schnappinger, R. de Vivie-Riedle and S. Mukamel, Visualizing conical intersection passages via vibronic coherence maps generated by stimulated ultrafast x-ray Raman signals, *Proc. Natl. Acad. Sci.*, 2020, **117**, 24069–24075.
40 S. M. Cavaletto, D. Keefer and S. Mukamel, High temporal and spectral resolution of stimulated x-ray Raman signals with stochastic free-electron-laser pulses, *Phys. Rev. X*, 2021, **11**, 011029.
41 D. Keefer, V. M. Freixas, H. Song, S. Tretiak, S. Fernandez-Alberti and S. Mukamel, Monitoring molecular vibronic coherences in a bichromophoric molecule by ultrafast x-ray spectroscopy, *Chem. Sci.*, 2021, **12**, 5286–5294.
42 V. M. Freixas, S. Fernandez-Alberti, D. V. Makhov, S. Tretiak and D. Shalashilin, An ab initio multiple cloning approach for the simulation of photoinduced dynamics in conjugated molecules, *Phys. Chem. Chem. Phys.*, 2018, **20**, 17762–17772.
43 D. V. Makhov, W. J. Glover, T. J. Martinez and D. V. Shalashilin, Ab initio multiple cloning algorithm for quantum nonadiabatic molecular dynamics, *J. Chem. Phys.*, 2014, **141**, 054110.
44 S. Fernandez-Alberti, D. V. Makhov, S. Tretiak and D. V. Shalashilin, Non-adiabatic excited state molecular dynamics of phenylene ethynylene dendrimer using a multiconfigurational Ehrenfest approach, *Phys. Chem. Chem. Phys.*, 2016, **18**, 10028–10040.
45 S. Fernandez-Alberti, A. E. Roitberg, V. D. Kleiman, T. Nelson and S. Tretiak, Shishiodoshi unidirectional energy transfer mechanism in phenylene ethynylene dendrimers, *J. Chem. Phys.*, 2012, **137**, 22A526.

46 T. Nelson, S. Fernandez-Alberti, A. E. Roitberg and S. Tretiak, Electronic delocalization, vibrational dynamics, and energy transfer in organic chromophores, *J. Phys. Chem. Lett.*, 2017, **8**, 3020–3031.
47 D. Ondarse-Alvarez, S. Komurlu, A. E. Roitberg, G. Pierdominici-Sottile, S. Tretiak, S. Fernandez-Alberti and V. D. Kleiman, Ultrafast electronic energy relaxation in a conjugated dendrimer leading to inter-branch energy redistribution, *Phys. Chem. Chem. Phys.*, 2016, **18**, 25080–25089.
48 D. Keefer and S. Mukamel, Selective enhancement of spectroscopic features by quantum optimal control, *Phys. Rev. Lett.*, 2021, **126**, 163202.
49 D. V. Shalashilin, Nonadiabatic dynamics with the help of multiconfigurational Ehrenfest method: Improved theory and fully quantum 24D simulation of pyrazine, *J. Chem. Phys.*, 2010, **132**, 244111.
50 K. Saita and D. V. Shalashilin, On-the-fly ab initio molecular dynamics with multiconfigurational Ehrenfest method, *J. Chem. Phys.*, 2012, **137**, 22A506.
51 D. V. Makhov, C. Symonds, S. Fernandez-Alberti and D. V. Shalashilin, Ab initio quantum direct dynamics simulations of ultrafast photochemistry with multiconfigurational Ehrenfest approach, *Chem. Phys.*, 2017, **493**, 200–218.
52 D. V. Shalashilin and M. S. Child, The phase space CCS approach to quantum and semiclassical molecular dynamics for high-dimensional systems, *Chem. Phys.*, 2004, **304**, 103–120.
53 D. V. Shalashilin, Multiconfigurational Ehrenfest approach to quantum coherent dynamics in large molecular systems, *Faraday Discuss.*, 2011, **153**, 105.
54 M. V. Berry, Quantal phase factors accompanying adiabatic changes, *Proc. R. Soc. London, Ser. A*, 1984, **392**, 103–120.
55 C. Mead and D. Truhlar, On the determination of born-Oppenheimer nuclear motion wave functions including complications due to conical intersections and identical nuclei, *J. Chem. Phys.*, 1979, **70**, 2284–2296.
56 S. Fernandez-Alberti, A. E. Roitberg, T. Nelson and S. Tretiak, Identification of unavoided crossings in nonadiabatic photoexcited dynamics involving multiple electronic states in polyatomic conjugated molecules, *J. Chem. Phys.*, 2012, **137**, 014512.
57 V. M. Freixas, A. J. White, T. Nelson, H. Song, D. V. Makhov, D. Shalashilin, S. Fernandez-Alberti and S. Tretiak, Nonadiabatic excited-state molecular dynamics methodologies: Comparison and convergence, *J. Phys. Chem. Lett.*, 2021, **12**, 2970–2982, pMID: 33730495.
58 D. V. Makhov, K. Saita, T. J. Martinez and D. V. Shalashilin, Ab initio multiple cloning simulations of pyrrole photodissociation: Tker spectra and velocity map imaging, *Phys. Chem. Chem. Phys.*, 2015, **17**, 3316–3325.
59 T. R. Nelson, A. J. White, J. A. Bjorgaard, A. E. Sifain, Y. Zhang, B. Nebgen, S. Fernandez-Alberti, D. Mozyrsky, A. E. Roitberg and S. Tretiak, Non-adiabatic excited-state molecular dynamics: Theory and applications for modeling photophysics in extended molecular materials, *Chem. Rev.*, 2020, **120**, 2215–2287.
60 W. Malone, B. Nebgen, A. White, Y. Zhang, H. Song, J. A. Bjorgaard, A. E. Sifain, B. Rodriguez-Hernandez, V. M. Freixas, S. Fernandez-Alberti, et al., Nexmd software package for non-adiabatic excited state molecular dynamics simulations, *J. Chem. Theory Comput.*, 2020, **16**, 5771–5783.
61 H. Song, V. M. Freixas, S. Fernandez-Alberti, A. J. White, Y. Zhang, S. Mukamel, N. Govind and S. Tretiak, An ab initio multiple cloning method for non-adiabatic excited-state molecular dynamics in nwchem, *J. Chem. Theory Comput.*, 2021, **17**, 3629–3643.
62 S. Tretiak and S. Mukamel, Density matrix analysis and simulation of electronic excitations in conjugated and aggregated molecules, *Chem. Rev.*, 2002, **102**, 3171–3212.
63 V. Chernyak, M. F. Schulz, S. Mukamel, S. Tretiak and E. V. Tsiper, Krylov-space algorithms for time-dependent Hartree–Fock and density functional computations, *J. Chem. Phys.*, 2000, **113**, 36–43.
64 S. Tretiak, C. M. Isborn, A. M. Niklasson and M. Challacombe, Representation independent algorithms for molecular response calculations in time-dependent self-consistent field theories, *J. Chem. Phys.*, 2009, **130**, 054111.
65 F. Furche and R. Ahlrichs, Adiabatic time-dependent density functional methods for excited state properties, *J. Chem. Phys.*, 2002, **117**, 7433–7447.
66 S. Tretiak and V. Chernyak, Resonant nonlinear polarizabilities in the time-dependent density functional theory, *J. Chem. Phys.*, 2003, **119**, 8809–8823.
67 M. Tommasini, V. Chernyak and S. Mukamel, Electronic density-matrix algorithm for nonadiabatic couplings in molecular dynamics simulations, *Int. J. Quantum Chem.*, 2001, **85**, 225–238.
68 V. Chernyak and S. Mukamel, Density-matrix representation of nonadiabatic couplings in time-dependent density functional (tddft) theories, *J. Chem. Phys.*, 2000, **112**, 3572–3579.
69 R. Send and F. Furche, First-order nonadiabatic couplings from time-dependent hybrid density functional response theory: Consistent formalism, implementation, and performance, *J. Chem. Phys.*, 2010, **132**, 044107.
70 M. J. Dewar, E. G. Zoebisch, E. F. Healy and J. J. Stewart, Development and use of quantum mechanical molecular models. 76. am1: a new general purpose quantum mechanical molecular model, *J. Am. Chem. Soc.*, 1985, **107**, 3902–3909.
71 S. Mukamel, S. Tretiak, T. Wagersreiter and V. Chernyak, Electronic coherence and collective optical excitations of conjugated molecules, *Science*, 1997, **277**, 781–787.
72 S. Tretiak, V. Chernyak and S. Mukamel, Recursive density-matrix-spectral-moment algorithm for molecular nonlinear polarizabilities, *J. Chem. Phys.*, 1996, **105**, 8914–8928.
73 S. Tretiak, W. M. Zhang, V. Chernyak and S. Mukamel, Excitonic couplings and electronic coherence in bridged naphthalene dimers, *Proc. Natl. Acad. Sci.*, 1999, **96**, 13003–13008.

74 V. M. Freixas, D. Ondarse-Alvarez, S. Tretiak, D. V. Makhov, D. V. Shalashilin and S. Fernandez-Alberti, Photoinduced non-adiabatic energy transfer pathways in dendrimer building blocks, *J. Chem. Phys.*, 2019, **150**, 124301.

75 J. Wang, R. M. Wolf, J. W. Caldwell, P. A. Kollman and D. A. Case, Development and testing of a general amber force field, *J. Comput. Chem.*, 2004, **25**, 1157–1174.

76 A. L. Thompson, C. Punwong and T. J. Martínez, Optimization of width parameters for quantum dynamics with frozen gaussian basis sets, *Chem. Phys.*, 2010, **370**, 70–77.

Supplementary information

Ultrafast coherent photoexcited dynamics in a trimeric dendrimer probed by X-ray stimulated-Raman signals

Victor M. Freixas[†1], Daniel Keefer[†2], Sergei Tretiak[3], Sebastian Fernandez-Alberti[1], Shaul Mukamel[*2]

[1] *Departamento de Ciencia y Tecnologia, Universidad Nacional de Quilmes/CONICET, B1876BXD, Bernal, Argentina*
[2] *Department of Chemistry and Physics and Astronomy, University of California, Irvine, California 92697-2025, USA*
[3] *Theoretical Division, Los Alamos National Laboratory, Los Alamos, New Mexico 87545, United States*

[†] These authors contributed equally

[*]smukamel@uci.edu

Contents

A Cloning criteria and thresholds

- *Criteria #1:*

  Cloning should take pace in situations where more than one excited state is significantly populated. This can be monitored by the distribution width W_n[1]:

$$W_n = \frac{1}{\sum_I^N \left|a_I^{(n)}\right|^4} \quad . \tag{S1}$$

  W_n takes values between 1 and the total number of excited states considered N. Values near 1 means that all the population is concentrated in a single state, while values near N means an even distribution. Therefore, the cloning events were restricted to situations where:

$$W_n > \delta_1 = 2.0 \quad . \tag{S2}$$

  The time evolution of the expectation value of W_n might be misleading in the sense that it has a broad distribution and presents sudden changes after cloning events. Moreover, it only quantifies whether the electronic populations for a given trajectory spread over the different states or not. A more decisive criterion is the breaking angle defined in criteria #2: the populations might be distributed over several states, but if all those states pull the nuclear system in the same direction of motion there is no need for bifurcating the wavefunction. Figure S1 depicts the distribution of values of W_n for all time steps and trajectories of the complete ensemble for the current case. The peak at approximately $W_n = 2$ is associated to the threshold $\delta_1 = 2$, while the peak at approximately $W_n = 1$ is associated either to the subsequent reduction of W_n after each cloning event or to values acquired after electronic energy relaxation to the S_1 state.

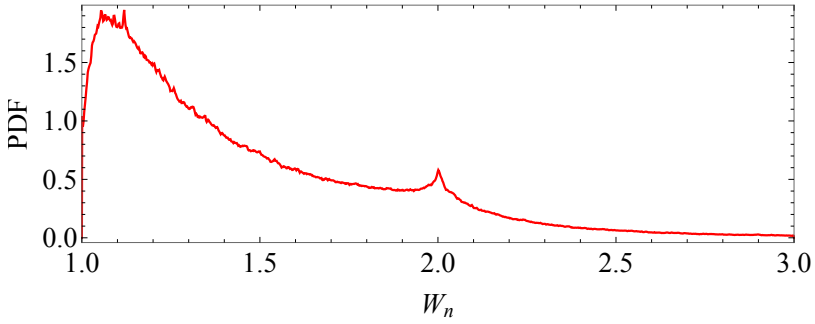

Figure S1: Probability density function (PDF) of W_n defined according to (eq. S1) for all trajectories and time steps of the complete ensemble for the current case.

- *Criteria #2:*

  Cloning should take place in situations where the wavepacket would split in configuration space. This is monitored by the breaking angle [1]:

$$\theta^{(n)} = \arccos\left(\frac{2\mathbf{F}_M^{(n)} \cdot \mathbf{F}_{max}^{(n)}}{\left|\mathbf{F}_M^{(n)}\right|^2 + \left|\mathbf{F}_{max}^{(n)}\right|^2}\right) \quad , \tag{S3}$$

where $\mathbf{F}_M^{(n)}$ is the averaged excited state gradient for configuration n:

$$\mathbf{F}_M^{(n)} = -\sum_I \left|a_I^{(n)}\right|^2 \nabla_{\mathbf{R}_n} V_I^{(n)} \quad , \tag{S4}$$

where $\mathbf{R}_n$ represents the nuclear coordinates for configuration n and $V_I^{(n)}$ represents the energy corresponding to the excited state I of configuration n. $\mathbf{F}_{max}^{(n)}$ is minus the gradient corresponding to the most populated state. By restricting the cloning events to situations in which:

$$\theta^{(n)} > \delta_2 = 10^\circ \quad , \tag{S5}$$

we ensure that the two new configurations produced after a cloning event will split in configuration space providing the desired bifurcation effect and rectifying the physical meaning of the mean field.

- *Criteria #3:*

  In order to make the algorithm efficient and avoid a overproduction of cloning events in the strong coupling regions of configuration space, we avoid cloning when the coupling is to high. By this way clones are produced once the system leaves strong coupling regions if the two previous criteria are fulfilled. The coupling is monitored in similar fashion as the quantum transition probability is calculated for the fewest switches surface hopping algorithm [2, 3]:

$$\sum_I \left| \frac{2\sigma_I^{(n)} \cos\left(\theta_I^{(n)} - \theta_{max}^{(n)}\right) \dot{\mathbf{R}}_n \cdot \mathbf{d}_{I,max}^{(n)}}{\sigma_{max}} \right| < \delta_3 \quad , \tag{S6}$$

  where $\sigma_I^{(n)}$ and $\theta_I^{(n)}$ are the modulus and phase corresponding to the electronic amplitudes $a_I^{(n)}$, the index max refers to the most populated state, $\dot{\mathbf{R}}_n$ is the nuclear velocity in configuration n and $\mathbf{d}_{I,max}^{(n)}$ is the non-adiabatic coupling between excited states I and the one with the greater population for configuration n:

$$\mathbf{d}_{I,max}^{(n)} = \langle \phi_I^{(n)} \left| \nabla_{\mathbf{R}_n} \right| \phi_{max}^{(n)} \rangle \quad . \tag{S7}$$

  Therefore, by setting $\delta_3 = 0.05$ we ensure an efficient clone generation away from the strong coupling regions of configuration space.

- *Criteria #4:*

  The nuclear amplitude corresponding to each configuration splits after a cloning event. If the total number of clones is not controlled, an exponential growth, with an exponentially decreasing weight for the corresponding configurations, would make the algorithm too inefficient. Therefore, we allowed a total of 4 consecutive clones, leading to a maximum of 16 clones per initial condition. Previous convergence tests have shown that there is no a relevant accuracy improvement after the production of approximately 14 clones per initial condition [2]. In the current case, an average of approximately 6 clones per initial condition were generated. These clones take place through out all the simulation time. Figure S2 shows that cloning events occurs during the simulations in an homogeneous rate.

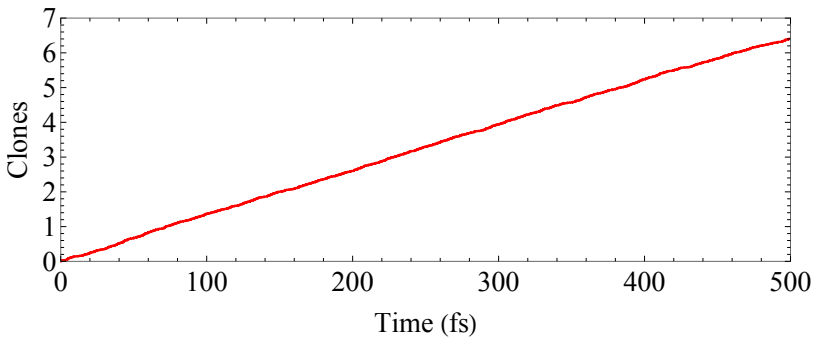

Figure S2: Average number of cloning events per initial condition as a function of time.

B Fraction of transition density

Within the Collective Electronic Oscillator (CEO) approach the Configuration Interaction Singlet (CIS) eigenstate I for configuration n, written in Atomic Orbitals (AO) basis, is denoted frequently as transition density matrices [4, 5, 6]:

$$\left(\rho_I^{(n)}\right)_{i,j} = \langle \phi_I^{(n)} \left| \hat{c}_i^\dagger \hat{c}_j \right| \phi_g^{(n)} \rangle \quad , \tag{S8}$$

where $|\phi_g^{(n)}\rangle$ is the ground state wavefunction, and $\hat{c}_i^\dagger$ and $\hat{c}_j$ are the electron creation and annhilation operators with indexes i and j referring to AO basis functions. Diagonal elements $\left(\rho_I^{(n)}\right)_{i,i}$ are relevant to the changes in the distribution of electronic density in the ith orbital in the case of bound excitonic states caused by excitation [7].

During AIMC simulations, the intramolecular electronic energy redistribution can be followed using the time-dependent spatial localization of $\rho_I^{(n)}$. The fraction of transition density localized on a specific segment X of the molecule can be defined as [1]:

$$\rho_{I,X}^{(n)} = \frac{\sum_{i \in X} \left(\rho_I^{(n)}\right)_{i,i}^2}{\sum_i \left(\rho_I^{(n)}\right)_{i,i}^2} \quad . \tag{S9}$$

In order to calculate the corresponding expectation value for the Multiconfigurational Ehrenfest (MCE) wavefunction we can introduce the operator $\hat{\rho}_X$ such that:

$$\hat{\rho}_X |\phi_I^{(n)}\rangle = \rho_{I,X}^{(n)} |\phi_I^{(n)}\rangle \quad , \tag{S10}$$

which expectation value can be calculated as:

$$\langle \hat{\rho}_X \rangle = \Re \left\{ \sum_{n,m} c_m^* c_n \langle \chi_m | \chi_n \rangle \sum_{I,J} \left(a_I^{(m)}\right)^* a_J^{(n)} \langle \phi_I^{(m)} | \phi_J^{(n)} \rangle \rho_{I,X}^{(m)} \right\} \quad , \tag{S11}$$

where $\Re$ stands for the real part.

C Parameters of the fit to eq. (1)

The function in eq. (1) describes the relaxation process to S_1 as a superposition of an exponential decay plus an exponentially damped oscillation, such that both contributions have the same weight at $t = 0$. Parameters a and b corresponds to the asymptotic value of S_1 population and its initial value, respectively; τ_1 is the S_1 decay time, T is the period of the vibronic oscillations and τ_2 is the vibronic decoherence time. R is the corresponding R-squared.

Parameter	Estimate	Standard error
a	0.81	0.00
b	0.24	0.00
$\tau_1(fs)$	5.42	0.04
$T(fs)$	19.96	0.02
$\tau_2(fs)$	23.31	0.12
R	0.9999	–

Table S1: Parameters obtained by fitting the population of S_1 in Figure 2(a) to $f(t)$ given by eq. (1).

D Pure electronic dephasing

Within linear response theory [8], the correlation between excited states I and J is quantified by the autocorrelation function:

$$C_{IJ} = \langle \delta E_{IJ}(t) \delta E_{IJ}(0) \rangle, \tag{S12}$$

where δE_{IJ} is the corresponding energy gap and the angular brackets means average over the ensemble. The energy corresponding to a given state K is calculated as the expectation value:

$$\begin{aligned} E_K &= \langle \Psi | \hat{E}_K | \Psi \rangle = \\ &= \sum_{n,m} (c_m)^* \, c_n \langle \chi_m | \chi_n \rangle E_K^{(n)} \sum_{IJ} \left(a_I^{(m)} \right)^* a_J^{(n)} \langle \phi_I^{(m)} | \phi_J^{(n)} \rangle, \end{aligned} \tag{S13}$$

where $E_K^{(n)}$ is the energy corresponding to the adiabatic state K for the center of configuration n.

The pure electronic dephasing $D_{IJ}(t)$ is defined by the second order cumulant approximation [8]:

$$D_{IJ} = \exp\left(-\frac{1}{\hbar^2} \int_0^t dt' \int_0^{t'} dt'' C_{IJ}(t) \right). \tag{S14}$$

Finally, the pure electronic decoherence time τ_{IJ} can be obtained by fitting the pure dephasing D_{IJ} to a Gaussian function:

$$D_{IJ} \approx \exp\left(-\left(\frac{t}{\tau_{IJ}} \right) \right). \tag{S15}$$

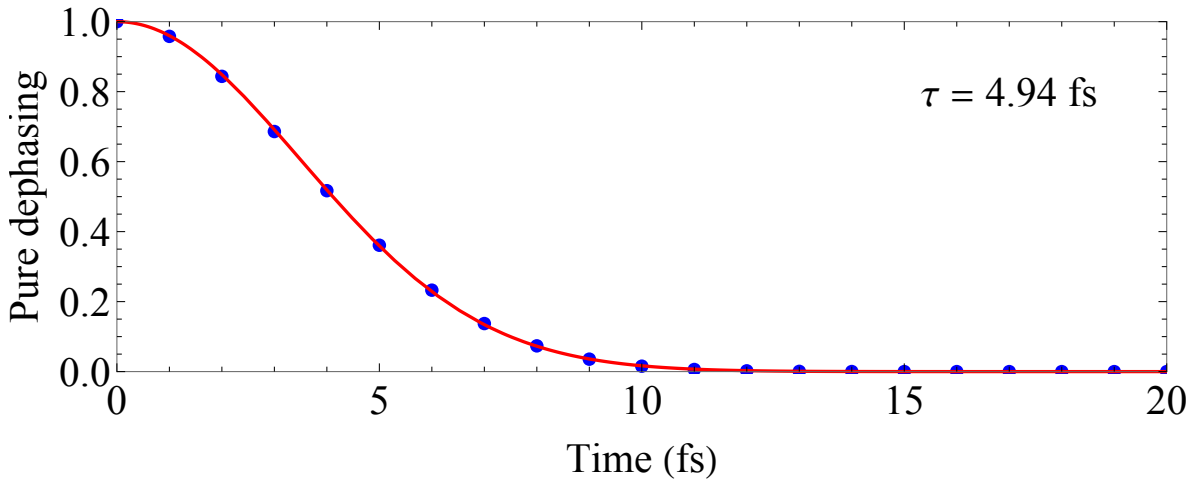

Figure S3: Pure electronic dephasing function for the triarylamine trimer $D_{12}(t)$ evaluated from the AIMC simulations.

E Surface hopping simulations

NEXMD surface hopping (SH) simulations were performed in order to compare the capability of the SH method to reproduce the oscillatory behavior of the electronic populations resulting from vibronic coherences. The same ensemble of initial configurationshas as for AIMC simulations has been considered . The electronic wavefunction was collapsed to S_2 at $t = 0$ in order to maximize the appearance of any possible oscillations. Figure (S4) shows the electronic populations, calculated as the fraction of trajectories evolving on each state at any given time. NEXMD-SH simulations were performed at a constant energy. Classical time steps of 0.1 fs have been used for the propagation of nuclei in ground state and a quantum time step of 0.025 fs has been used to propagate the electronic degrees of freedom. Corrections for decoherence [9], parameters and the methodology of NEXMD-SH simulations have been extensively discussed elsewhere [10].

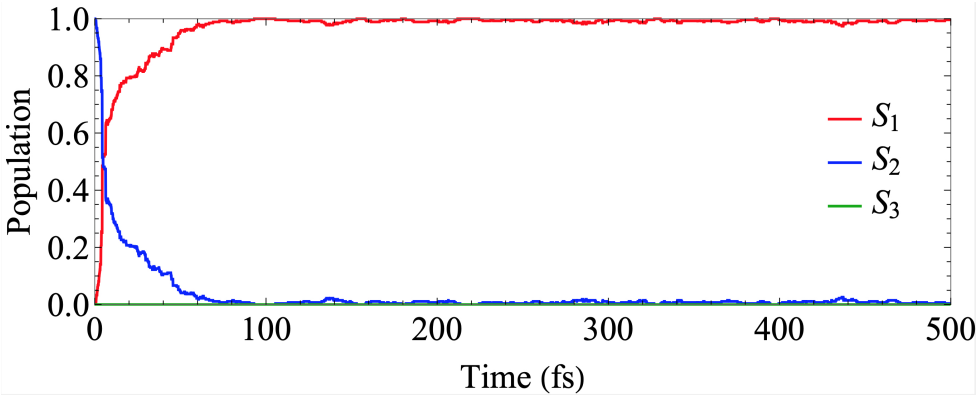

Figure S4: Time evolution of the electronic populations for SH dynamics.

F Transition density matrix snapshots

In order to calculate transition density matrix for the MCE wavefunction $|\Psi\rangle$, we first calculate the expectation value of the transition density matrix from the ground state to a given state K:

$$\rho_K = \langle\Psi|\hat{\rho}_{0K}|\Psi\rangle = \\ = \sum_{n,m} (c_m)^* \, c_n \langle\chi_m|\chi_n\rangle \rho_{0K}^{(n)} \sum_{IJ} \left(a_I^{(m)}\right)^* a_J^{(n)} \langle\phi_I^{(m)}|\phi_J^{(n)}\rangle, \tag{S16}$$

where $\rho_{0K}^{(n)}$ is the transition density matrix [7] from the ground state to excited state K for the center of configuration n.

The transition density matrix ρ from the ground state to the superposition of excited states is then calculated as:

$$\rho = \sum_K |a_K|^2 \rho_K, \tag{S17}$$

where a_K is calculated according to [1]:

$$|a_K|^2 = \Re\left\{ \sum_{n,m} (c_m)^* \, c_n \langle\chi_m|\chi_n\rangle \left(a_K^{(m)}\right)^* \sum_I a_I^{(n)} \langle\phi_K^{(m)}|\phi_I^{(n)}\rangle \right\}. \tag{S18}$$

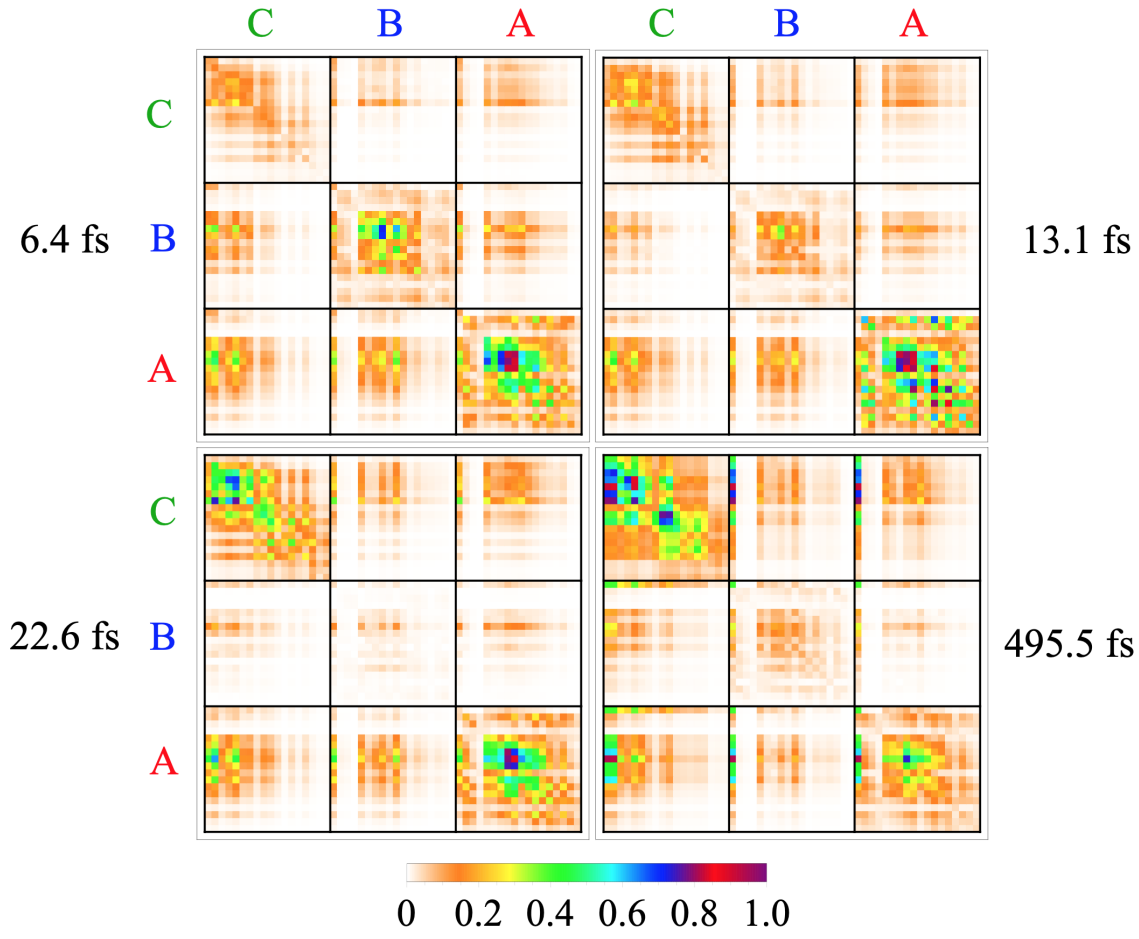

Figure S5: Transition density matrices (eq. (S17)) corresponding to the the different snapshots shown in Figure 3(a).

G Non-adiabatic coupling analysis

A further insight into the vibronic dynamics can be achieved by analyzing the nonadiabatic coupling vector (NACR) in regions of strong coupling near conical intersection seams. The strong coupling regime is defined as situations where the absolute value of NACR is higher than its mean value plus 10 times the standard deviation during each AIMC trajectory. Figure S6(a) shows a real-space representation of a typical NACR. We find that NACR involves antisymmetric nuclear motions on two of the three branches. This behavior involving antisymmetric motions on different branches of a dendrimer has been reported previously [11] and was associated to the fact that the molecular wavefunction adopts a standing wave pattern according to the particle (exciton) in a box model and the $S_2 \rightarrow S_1$ transition can be associated with a transition where symmetry between states changes. That is, the vibronic excitation has an antisymmetric form where the two branches experience structural deformations with opposite phases (i.e. expansion and compression). Figure S6(b) depicts the probability density function of the fraction of NACR absolute values localized on the three branches, denoted as I, II, and III according to their corresponding contribution values in a decreasing order. We can observe that the NACRs are not equally distributed among the three branches but localized mainly in two of them. The distribution of the projections of NACR onto the normal modes basis, calculated at the S_1 minimum energy configuration, is shown in Figure S6(c). The peak at $\sim$ 19 fs ($\sim$ 1750 cm^{-1}) matches the period T of the vibronic oscillations ($\sim$ 20 fs) obtained by fitting the evolution in time of the S_1 population (see Figure 2(a) and Table S1). Vibronic dynamics are thus assisted by a reduced set of high-frequency normal modes.

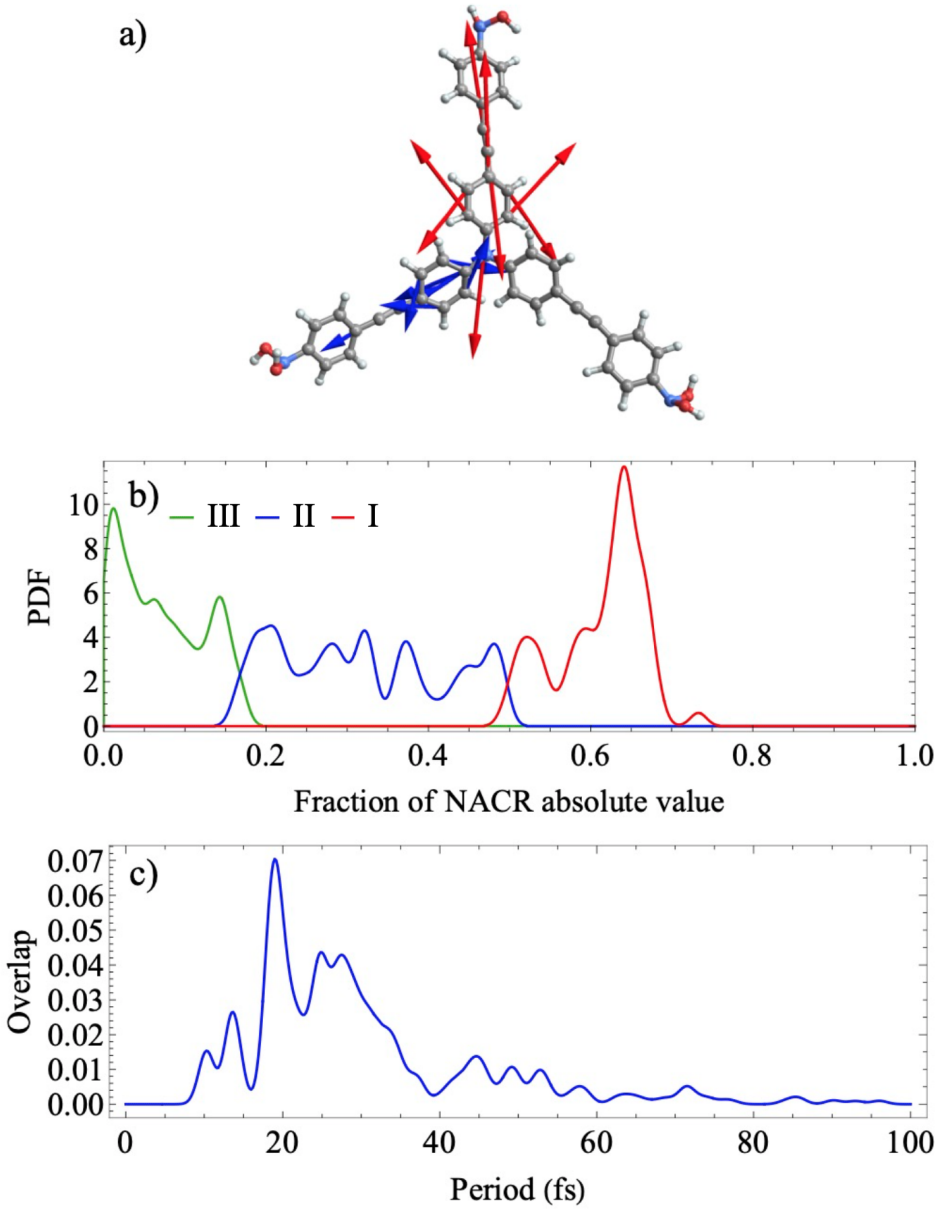

Figure S6: **(a)** Representation of a typical NACR in real space during a region of strong coupling between states. **(b)** Probability density function of the fraction of NACR absolute values during strong coupling regime. For each AIMC trajectory, branches I, II, and III are sorted according to their corresponding fractions of NACR absolute value in decreasing order. **(c)** Distribution of the overlap between nuclear normal modes, calculated at the S_1 minimum energy configuration, and the NACR at configurations of strong coupling.

H Additional Trajectories

Only trajectory 2 is discussed in the main text. This trajectory is representative of a large fraction of trajectories in the ensemble, with only minor differences especially in the signal. Here, we discuss a few interesting trajectories to give a better impression about the range of properties during the dynamics.

- Figure S7 shows a trajectory that is similar to trajectory 2 in the main text, but where the transition density is located in branches A and C instead of B and C. This exemplifies that most trajectories are quite similar and the three branches of the molecule are equal, while the transition density is localized in two of them simultaneously.
- Figure S8 depicts a trajectory where the ρ_{13} contribution to the signal is equally strong to the usually dominating ρ_{12} contribution. Thus, they are both well visible in the total signal of this trajectory and well distinguishable at different Raman shifts.
- In Figure S9, trajectory 5 exhibits much larger and more frequent population oscillations, especially between S_1 and S_2. This does not considerably affect the relative magnitudes and persistence of the individual signal contributions, however.

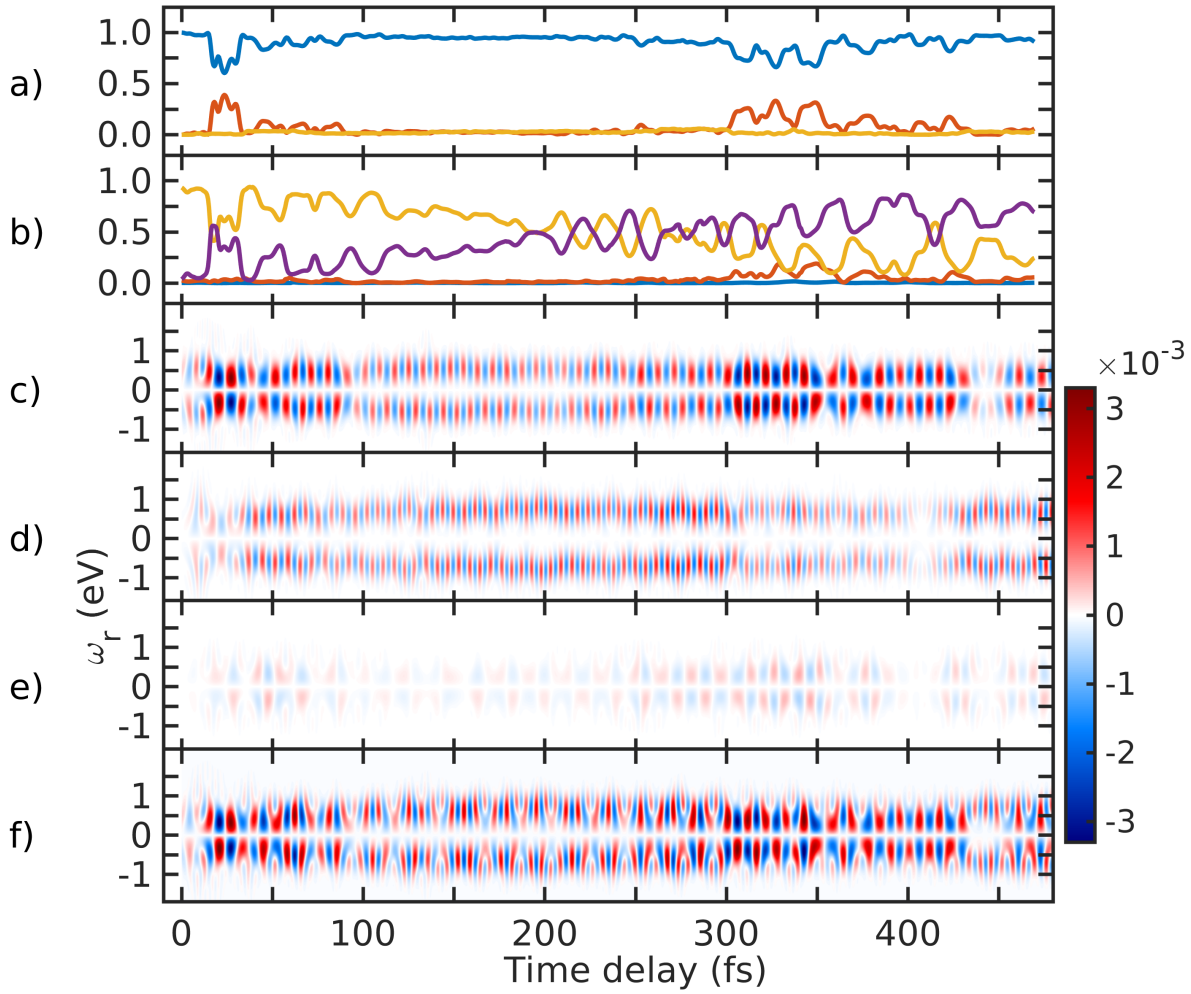

Figure S7: Dynamics and TRUECARS signal in trajectory 3. **a)** Populations in the S_1 (blue), S_2 (red) and S_3 (yellow) states. **b)** Fraction of transition density in branch A (purple), B (yellow), C (red) and around the central Nitrogen (blue). **c)** Frequency-dispersed TRUECARS signal (eq. 2) for the coherence ρ_{12} between S_1 and S_2. **d–e)** same as c) for ρ_{13} and ρ_{23}. **f)** Total TRUECARS signal for trajectory 2 given by the sum of c–e.

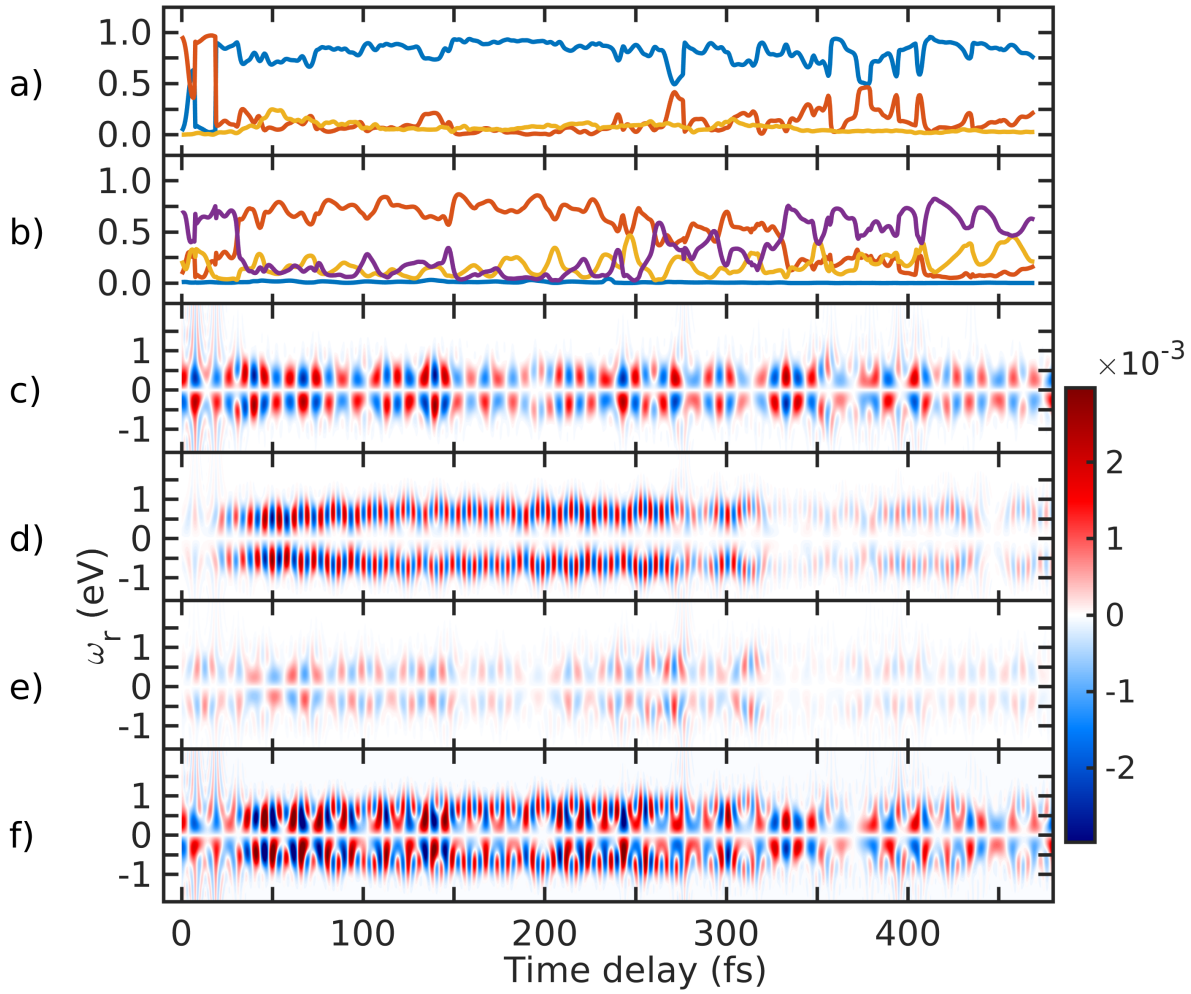

Figure S8: Dynamics and TRUECARS signal in trajectory 4. **a)** Populations in the S_1 (blue), S_2 (red) and S_3 (yellow) states. **b)** Fraction of transition density in branch A (purple), B (yellow), C (red) and around the central Nitrogen (blue). **c)** Frequency-dispersed TRUECARS signal (eq. 2) for the coherence ρ_{12} between S_1 and S_2. **d–e)** same as c) for ρ_{13} and ρ_{23}. **f)** Total TRUECARS signal for trajectory 2 given by the sum of c–e.

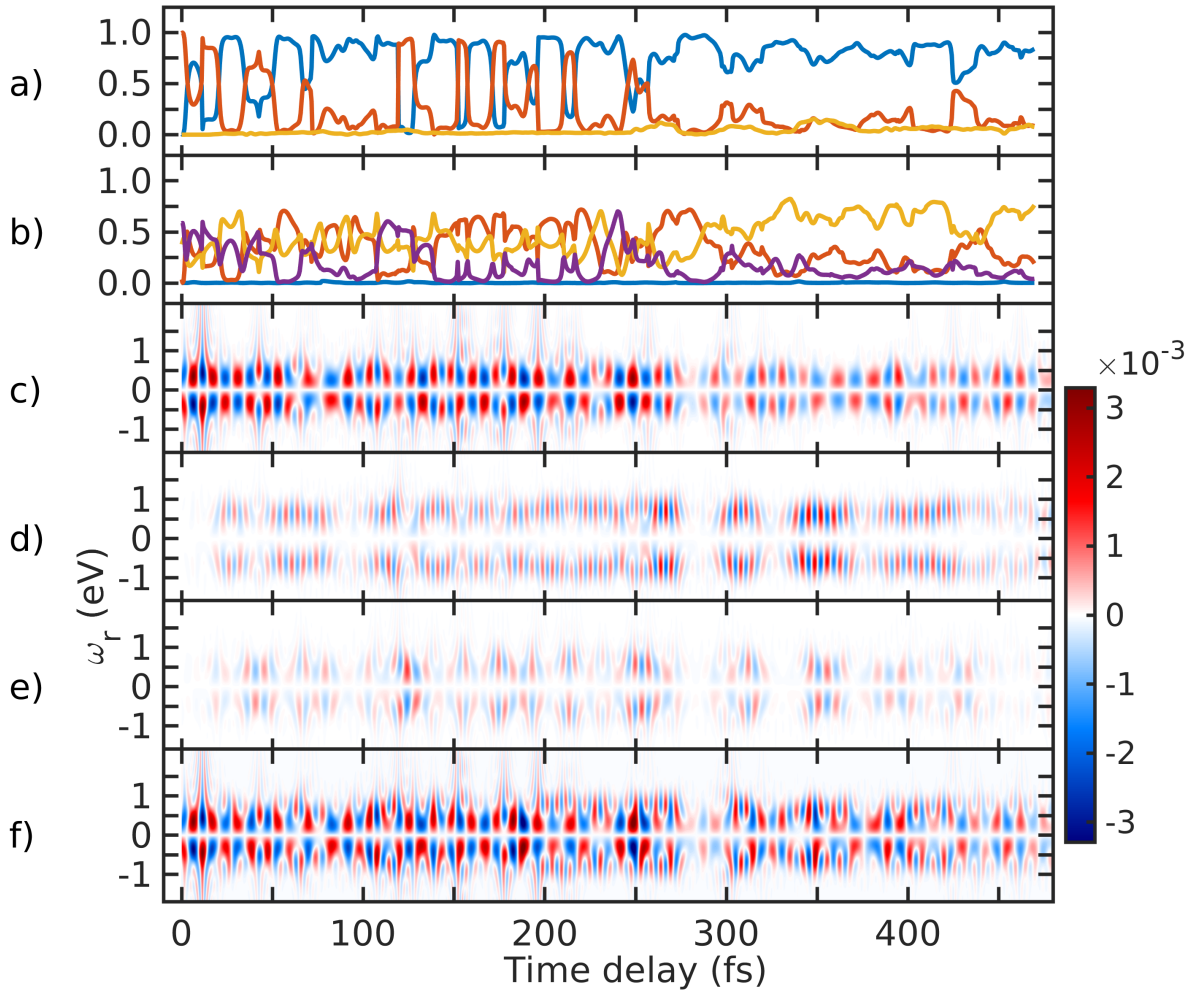

Figure S9: Dynamics and TRUECARS signal in trajectory 5. **a)** Populations in the S_1 (blue), S_2 (red) and S_3 (yellow) states. **b)** Fraction of transition density in branch A (purple), B (yellow), C (red) and around the central Nitrogen (blue). **c)** Frequency-dispersed TRUECARS signal (eq. 2) for the coherence ρ_{12} between S_1 and S_2. **d–e)** same as c) for ρ_{13} and ρ_{23}. **f)** Total TRUECARS signal for trajectory 2 given by the sum of c–e.

I Frenkel exciton model

In the Frenkel exciton model, the excited states of the trimer are considered as a linear combination of the solutions for the individual branches. In the perfect symmetry regime, and using the first solution E on each identical branch and a unique common coupling V between them as a basis, the Frenkel exciton Hamiltonian can be expressed as:

$$H = \begin{pmatrix} E & V & V \\ V & E & V \\ V & V & E \end{pmatrix}, \tag{S19}$$

with eignevalues:

$$\begin{matrix} E - V \\ E - V \\ E + 2V \end{matrix} \tag{S20}$$

and eigenvectors:

$$\begin{matrix} (-1 & 0 & 1) \\ (-1 & 1 & 0) \\ (\ 1 & 1 & 1) \end{matrix} \tag{S21}$$

If we associate the S_1 and S_2 to the degenerate states with energies $E - V$, and S_3 with energy $E + 2V$, the coupling V can be estimated as one third of the energy splitting between S_1/S_2 and S_3.

References

[1] Victor M. Freixas, Sebastian Fernandez-Alberti, Dmitry V. Makhov, Sergei Tretiak, and Dmitrii Shalashilin. An ab initio multiple cloning approach for the simulation of photoinduced dynamics in conjugated molecules. *Phys. Chem. Chem. Phys.*, 20:17762–17772, 2018.

[2] Victor M. Freixas, Alexander J. White, Tammie Nelson, Huajing Song, Dmitry V. Makhov, Dmitrii Shalashilin, Sebastian Fernandez-Alberti, and Sergei Tretiak. Nonadiabatic excited-state molecular dynamics methodologies: Comparison and convergence. *The Journal of Physical Chemistry Letters*, 12(11):2970–2982, 2021. PMID: 33730495.

[3] Daniel Keefer, Victor M. Freixas, Huajing Song, Sergei Tretiak, Sebastian Fernandez-Alberti, and Shaul Mukamel. Monitoring molecular vibronic coherences in a bichromophoric molecule by ultrafast x-ray spectroscopy. *Chem. Sci.*, 12:5286–5294, 2021.

[4] Shaul Mukamel, Sergei Tretiak, Thomas Wagersreiter, and Vladimir Chernyak. Electronic coherence and collective optical excitations of conjugated molecules. *Science*, 277(5327):781–787, 1997.

[5] Sergei Tretiak, Vladimir Chernyak, and Shaul Mukamel. Recursive density-matrix-spectral-moment algorithm for molecular nonlinear polarizabilities. *The Journal of chemical physics*, 105(19):8914–8928, 1996.

[6] Sergei Tretiak, Wei Min Zhang, Vladimir Chernyak, and Shaul Mukamel. Excitonic couplings and electronic coherence in bridged naphthalene dimers. *Proceedings of the National Academy of Sciences*, 96(23):13003–13008, 1999.

[7] Sergei Tretiak and Shaul Mukamel. Density matrix analysis and simulation of electronic excitations in conjugated and aggregated molecules. *Chemical reviews*, 102(9):3171–3212, 2002.

[8] Shaul Mukamel. *Principles of nonlinear optical spectroscopy*, volume 29. Oxford university press New York, 1995.

[9] Tammie Nelson, Sebastian Fernandez-Alberti, Adrian. E. Roitberg, and Sergei Tretiak. Nonadiabatic excited-state molecular dynamics: Treatment of electronic decoherence. *Journal of Chemical Physics*, 138:224111, 2013.

[10] Tammie. R. Nelson, Alexander White, Josiah. A. J.; Bjorgaard, Andrew E. Sifain, Yu Zhang, Benjamin Nebgen, Sebastian Fernandez-Alberti, Dimitry Mozyrsky, Adrian E. Roitberg, and Sergei Tretiak. Non-adiabatic excited-state molecular dynamics: Theory and applications for modeling photophysics in extended molecular materials. *Chemical Review*, 120:2215–2287, 2020.

[11] Tammie R. Nelson, Dianelys Ondarse-Alvarez, Nicolas Oldani, Beatriz Rodriguez-Hernandez, Laura Alfonso-Hernandez, Johan F. Galindo, Valeria D. Kleiman, Sebastian Fernandez-Alberti, Adrian E. Roitberg, and Sergei Tretiak. Coherent exciton-vibrational dynamics and energy transfer in conjugated organics. *Nature Communications*, 9:2316, 2018.